ACS APPLIED MATERIALS & INTERFACES

www.acsami.org

Research Article

Periodontal Ligament-Mimetic Fibrous Scaffolds Regulate YAP-Associated Fibroblast Behaviors and Promote Regeneration of Periodontal Defect in Relation to the Scaffold Topography

Jeong In Kim, Ju Yeon Kim, Govinda Bhattarai, Han-Sol So, Sung-Ho Kook,* and Jeong-Chae Lee*

Cite This: *ACS Appl. Mater. Interfaces* 2023, 15, 599−616

Read Online

ACCESS | Metrics & More | Article Recommendations | Supporting Information

ABSTRACT: Although multiple regenerative strategies are being developed for periodontal reconstruction, guided periodontal ligament (PDL) regeneration is difficult because of its cellular and fibrous complexities. Here, we manufactured four different types of PDL-mimic fibrous scaffolds on a desired single mat. These scaffolds exhibited a structure of PDL matrix and human PDL fibroblasts (PDLFs) cultured on the scaffolds resembling morphological phenotypes present in native PDLF. The scaffold-seeded PDLF exerted proliferative, osteoblastic, and osteoclastogenic potentials depending on the fiber topographical cues. Fiber surface-regulated behaviors of PDLF were correlated with the expression patterns of yes-associated protein (YAP), CD105, periostin, osteopontin, and vinculin. Transfection with si-RNA confirmed that YAP acted as the master mechanosensing regulator. Of the as-spun scaffolds, aligned or grid-patterned microscale scaffold regulated the YAP-associated behavior of PDLF more effectively than nanomicroscale or random-oriented microscale scaffold. Implantation with hydrogel complex conjugated with microscale-patterned or grid-patterned scaffold, but not other types of scaffolds, recovered the defected PDL with native PDL-mimic cellularization and fiber structure in the reformed PDL. Our results demonstrate that PDL-biomimetic scaffolds regulate topography-related and YAP-mediated behaviors of PDLF in relation to their topographies. Overall, this study may support a clinical approach of the fiber−hydrogel complex in guided PDL regenerative engineering.

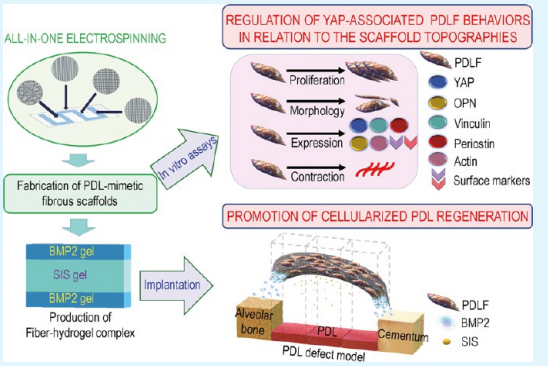

KEYWORDS: *PDL-mimetic fibrous scaffold, fiber−hydrogel complex, PDL fibroblasts, yes-associated protein 1, mechanosensitive cellular behavior, PDL regeneration*

1. INTRODUCTION

Periodontitis is a chronic inflammatory disease that destructs hard and soft tissues in the periodontium and eventually leads to tooth loss.[1−3] Although implant therapy or its combination with surgical grafting of alveolar bone and/or gum tissues is the most common treatment to restore tooth function, the long-term maintenance of osseointegrated dental implants is dependent on the health condition of the periodontium.[4] In the periodontium, periodontal ligament (PDL) plays crucial roles as the anatomical and functional biointerface. The abnormal structure and function of the PDL not only increase the risk of dental implant failure but also disturb alveolar bone remodeling in response to mechanical stimulation.[5] In some cases, the hypercalcification of PDL is also the cause of implant failure.[6] Therefore, the structural and functional maintenance of PDL are prerequisites for the long-term survival of the implants, as well as for the reconstruction of the periodontium.

PDL is an aligned fibrous connective tissue that tightly attaches cementum to the surrounding alveolar bone. PDL contains different types of bundled collagenous fibers such as Sharpey's and oxytalan fibers. Sharpey's fibers are vertically connected to the tooth and alveolar bone, whereas the oxytalan fibers run horizontally from the tooth and support blood vessels within the PDL.[5,7] Sharpey's fibers are also the major component of the extracellular matrix (ECM) and attach the periosteum to bone and muscle.[8,9] The rapid turnover and high remodeling properties of PDL are important for periodontal reconstruction, and these are orchestrated by the potential of Sharpey's and oxytalan fibers to sense physiological and mechanical stimuli and stimulate PDL fiber-attached cells.[10] PDL cells are a heterogeneous cell population composed of cementoblasts, endothelial and epithelial cells, fibroblasts, osteoblasts, and osteoclasts.[11,12] Of these cells, fibroblasts are the most abundant and predominant type in the PDL, and a

Received: October 20, 2022
Accepted: December 16, 2022
Published: December 28, 2022

proportion (1−5%) are undifferentiated cells known as PDL stem cells (PDLSCs).[13−15] Numerous studies have shown that PDL fibroblasts (PDLF) play essential roles in maintaining PDL integrity, mediating mechanosensing signals, and regulating alveolar bone remodeling.[13−16]

Currently, various biocompatible and biomimetic scaffolds in combination with stem cells have been developed for guided tissue engineering.[17] Strategies that induce in situ or multiple tissue regeneration with integrative structure formation are also being introduced.[18,19] As the periodontium is a complex composed of alveolar bone, gingiva, PDL, and tooth, the multiple tissue regenerative strategy is an ideal approach in dental clinics.[20−22] However, guided PDL regeneration is still challenging because of the complexity of PDL, which consists of various types of cells and collagenous fibers. Dissimilar to the surgical grafting of bone or bone-like biomaterials, the direct implantation of native PDL and its successful maintenance in the periodontium are difficult. Therefore, the development of an optimized PDL-biomimetic fibrous scaffold that specifically controls the behavior of PDL cells and recovers PDL function is important for efficient and successful PDL reparation.

We recently designed a new electrospinning system that improves the conductivity of a patterned trunk microfiber for additional branched nanonet fiber patterning that stabilizes elongated nanonet fibers.[23] We showed that the novel as-spun setup allows the desired fabrication of various patterned fibrous scaffolds such as microscale-aligned (m-ALFS), microscale-grid/patterned (m-GPFS), and nanomicroscale-grid/patterned (nm-GPFS) fibrous scaffolds. Compared with randomly oriented microscale fibrous scaffold (m-ROFS), the patterned scaffolds exhibit an ECM-mimic microenvironment more accurately.[23,24] Some of the patterned scaffolds tightly regulate the mechanosensing and behavior of bone marrow mesenchymal stem cells (BMMSCs).[23] More importantly, we found that the patterned as-spun scaffolds, such as m-ALFS and m-GPFS, might resemble the morphology of Sharpey's fibers, oxytalan fibers, or both. The nm-GPFS also exhibits fiber pattern that mimics collagen fibrils, fibers, and/or oxytalan fibers under mechanical stress. Taken together, it is strongly suggested that the as-spun scaffolds may mimic the structure of native PDL fibers and induce a recellularized PDL reparation.

In this study, we designed an all-in-one electrospinning system to improve manufactural efficacies. The application of all-in-one electrospinning allowed an optimized production of patterned or randomly oriented microscale or nanomicroscale fibrous scaffolds at the desired location on a single mat. Among these as-spun products, patterned scaffolds represented the structures of native PDL fibers and tightly regulated PDLF behavior and the expression of mechanosensing molecules. Specifically, yes-associated protein 1 (YAP)-mediated mechanosignaling regulated the induction of osteopontin (OPN), a mechanoresponsive marker for PDL maintenance, and periostin, a PDL-specific marker in periodontal tissue remodeling. In addition, our results show that implantation with patterned fiber−hydrogel complex almost completely recovers a PDL defect in an animal model. The current findings highlight crucial roles of YAP on fiber topography-regulated cellular behaviors, as well as on fiber−hydrogel complex-enhanced reparation of defected PDL with normalized matrix. Overall, this study demonstrates how patterned scaffolds regulate the behavior of PDLF and recover a PDL defect, providing the bioadvantages of all-in-one electrospinning to fabricate native PDL-like biomaterials.

2. EXPERIMENTAL SECTION

2.1. Chemicals and Equipment. Polycaprolactone (PCL, average Mw ∼14,000), *N*,*N*,-dimethylformamide (DMF, 99.85%), tetrahydrofuran (THF, ≥99.9%), rat tail collagen, and 1,1,1,3,3,3-hexafluoroisopropanol (HFIP, ≥99%) were purchased from Sigma-Aldrich Co. LLC (St. Louis, MI). Copper-enameled wire, silkworm cocoons, polycarbonate sheet, and cellophane membrane were offered from Cosmogenetech Inc. (Seoul, South Korea). A single plastic nozzle (21 gauge), a nozzle adapter, a syringe (12 cc), a polyethylene tubing (1.6 mm), and other electrospinning accessories were obtained from Nano NC (Seoul, South Korea). The α-minimum essential medium (α-MEM), Dulbecco's modified Eagle's medium (DMEM), antibiotics, fetal bovine serum (FBS), and trypsin-EDTA (2.5%) were purchased from Thermo Fisher Scientific (Waltham, MA). Bovine serum albumin (BSA) was obtained from Hyclone Laboratories Inc. (Logan, UT). Fluorescein isothiocyanate-conjugated monoclonal STRO-1, CD90, and CD105 antibodies and phycoerythrin-conjugated monoclonal CD45 and CD146 antibodies were purchased from BD Biosciences (Franklin, NJ). The 4′,6-diamidino-2-phenylindole (DAPI) and monoclonal antibodies specific to YAP and type I collagen (COLI) were purchased from Santa Cruz Biotechnology (Santa Cruz, CA). Monoclonal vinculin, OPN, and receptor activator of nuclear factor-κB (RANKL) antibodies were obtained from Abcam (Cambridge, U.K.). Green fluorescent actin (Actin Green 488 ReadyProbes), rhodamine phalloidin (RP)-conjugated F-actin (R415), type I collagenase (17018029), and dispase II (17105041) were provided from Thermo Fisher Scientific. Bone morphogenetic protein 2 (BMP2)-conjugated gelatin-based hydrogel (BMP2 gel) and small intestine submucosa-based hydrogel (SIS gel) were obtained from Bioink Solution, Inc. (Daegu, South Korea). Unless otherwise noted, other chemicals were purchased from Sigma-Aldrich Co. LLC.

2.2. Manufacture and Characterization of All-In-One Electrospinning-Derived Fibrous Scaffolds. *2.2.1. All-In-One Electrospinning System.* This system was designed to optimize the fabrication of PDL-mimic fibrous scaffolds expressing patterned, grid/patterned, or randomly oriented fiber morphology with microscale, nanoscale, or both diameters on a single mat. Briefly, PCL solution (10 wt %) was prepared in a HFIP solvent and extruded at a flow rate of 800 μL/h using a syringe pump (NE300, NEW ERA, Farmingdale, NY). The engineered fibrillar microenvironments together with tunable mechanical and controllable architectures in the as-spun scaffolds were materialized by modifying a metallic rotating collector, a polycarbonate sheet, a copper wire, and/or a cellophane membrane. Electrospinning was performed at 16 kV with a tip-to-rotor distance of 15 cm under constant humidity (30 ± 2%) and temperature (20 ± 1 °C).

2.2.2. Morphological and Physicochemical Analyses. The morphology of as-spun scaffolds was determined by scanning electron microscopy (SEM; JSM-5900, JEOL, Japan), and fiber diameter was evaluated using the fast Fourier transform (FFT) method and an ImageJ software (Ver. 1.51, NIH, Bethesda, MD). The wetting properties of scaffolds were determined by measuring the water contact angle using the UNI-CAM system (Gitsoft, Seoul, South Korea). Electric field analysis was performed using a COMSOL Metaphysics Ver.5.5 added to an AC/DC electrostatic module under a Windows Vista operating system. Crystallization of scaffolds was confirmed by the two-dimensional X-ray diffractometer (2D-XRD; X'Pert Pro, Malvern Panalytical, United Kingdom).

2.3. Cell Cultures and Assays for Mechanosensing-Regulated Cell Behavior. *2.3.1. PDL Sample Preparation and Ethic Statements.* Rat PDL samples were obtained from the maxillary molars of male Sprague-Dawley rats (6 weeks old; Orient Bio, Daejeon, South Korea). This study used the animals strictly following the recommendations in the Guide for the Animal Care and Use of the Jeonbuk National University. All protocols were approved by the University Committee on Ethics in the Care and Use of Laboratory Animals (JBNU 2021-0146). Human PDL samples were offered from healthy patients (20−30 years old) who underwent orthodontic premolar extraction or removal of the third molar. Written informed consent for the use of tooth and PDL samples was obtained from all

https://doi.org/10.1021/acsami.2c18893
ACS Appl. Mater. Interfaces 2023, 15, 599−616

donors with approval by the Review Board of the Jeonbuk National University Hospital.

2.3.2. Morphological Analysis of PDL Samples. The morphology and diameter of native PDL fibers or cells were evaluated by SEM and transmission electron microscopy (TEM; JEM-2010, JEOL). To this end, rat and human PDL samples were fixed in PBS (pH 7.4) supplemented with 2% of paraformaldehyde and glutaraldehyde overnight at 4 °C. After washing with 0.05 M sodium cacodylate buffer, PDL samples were treated with 1% osmium tetroxide for 90 min followed by a dehydration step using the graded ethanol solution (50−100%). The PDL samples were infiltrated and embedded with various concentrations of propylene oxide (PO) and epoxy 812 resin (pristine PO, 1:1 PO/resin, 1:3 PO/resin, or neat resin). The embedded PDL samples were sectioned at a thickness of 60−70 nm using an ultramicrotome and observed by SEM or TEM. To further visualize the direction of PDL fibers, SEM and TEM images were converted into the corresponding color-coded images using Orientation J software.

2.3.3. Cultures of BMMSC and PDLF. BMMSCs were purchased from PromoCell GmbH (C-12974, Heidelberg, Germany) and cultured on scaffold-covered coverslips that were attached to the bottom of a 48-well tissue culture plate (TCP). BMMSCs were grown in α-MEM supplemented with 20% of FBS, 100 IU/mL of penicillin G, and 100 μg/mL of streptomycin at 37 °C in a humidified atmosphere of 5% CO_2. PDLFs were isolated from human teeth samples and cultured following the methods described previously with a slight modification.[14] Detailed procedures for PDLF preparation are provided in the Supporting Information. Both BMMSC and PDLF cultures were maintained at 37 °C in a humidified atmosphere with 5% CO_2 and switched to a fresh batch of the same medium every 3 days. These cells at the third passage were divided onto the scaffold-covered coverslips or the bottom of 48-well TCP (1×10^5 cells/well). Fiber topography-associated cellular phenotype and behavior such as proliferation, differentiation, morphological alteration, and mechanosensing in PDLF were evaluated and compared with that in BMMSC at various days of incubation.

2.3.4. Characterization of Surface Markers Expressed in PDLF. PDLFs at the first passage were harvested using 0.25% trypsin/EDTA buffer and fixed with 4% formaldehyde for 30 min. After washing with 0.2% of BSA-included PBS, cells were incubated for 30 min in PBS-containing antibodies specific to cell surface markers such as STRO-1, CD45, CD90, CD105, and CD146. Population of cells expressing these markers was analyzed by flow cytometry using an FACS Calibur flow cytometer (BD Biosciences) and FlowJo software (FlowJo, LLC, Ashland, OR).

2.3.5. Assays for the Fiber Topography-Related Morphological Alterations in PDLF. We evaluated how cytoplasmic phenotypes of PDLFs are affected in relation to fiber topographies of scaffolds by staining with green actin and RP-conjugated F-actin after 5 days of incubation. The morphology of the PDLF grown on scaffolds or TCP was observed by field emission-SEM (FE-SEM) (Gemini500, Carl Zeiss, Oberkochen, Germany). The intensities specific to green fluorescence and RP that indicate a characteristic elongation and the migration of cells along the fibers were observed by confocal laser scanning microscopy (CLSM, Carl Zeiss). To evaluate the cytoplasmic directionality and length of PDLF, the roundness, aspect ratio, and circularity were measured using NeuronJ plugin software. The formulas applied to calculate these parameters are shown in Figure S1. Fiber topography-associated alteration in the morphology of cultured PDLF was also determined by a false color-coded imaging in SEM images.

2.3.6. Immunofluorescence Staining and Imaging. PDLFs grown on scaffolds or TCP were fixed at 5 days post incubation and stained with anti-YAP, antivinculin, anti-OPN, anti-COLI, or antiperiostin antibody in a dilution of 1:200. These cells were treated with Alexa Fluor 488-conjugated antigoat IgG (1:500, Abcam), Alexa Fluor 633-conjugated antirabbit IgG (1:300, Abcam), or Alexa Fluor 594-conjugated antirabbit IgG (1:300, Abcam) and counterstained with DAPI. The relative expression intensity (a.u.) between YAP, vinculin, OPN, periostin, and/or COLI along with cytoplasmic phenotypes was determined by CLSM. YAP-specific intensity and cellular localization in cultured PDLF were determined at 5 days post incubation by CLSM after staining with anti-YAP antibody and DAPI. The nuclear size that means the distance from the bottom to the top nuclear edge was determined from CLSM images, in which imaging and data analysis in 2D were performed.[25] The relationship between YAP expression and cytoskeletal morphology was also evaluated by reconstructing CLSM images using ImageJ and ZEN microscope software. In addition, cellular YAP localization and intensity along with traction force in cultured PDLFs were also estimated by three-dimensional (3D) shape remodeling using a Z-stacking program. To estimate the cell infiltration of PDLF into the scaffolds, the 3D cell cross-sectional area (μm^2) was also measured by rotating (90°) 3D reconstructive CLSM images in the *X*-axis direction using the Z-stacking program.

2.3.7. Focal Adhesion (FA) Formation Assessment. The traction force exposed to PDLF was also evaluated by determining the penetration of these cells in relation to the pattern and scale of the fibers using SEM, as described previously.[23] Briefly, the average area and number of 3D-generated FAs in cultured PDLFs were analyzed using the Z-stack technique in the programs of ImageJ and ZEN (Figure S2). The images of vinculin-stained PDLF were subtracted by "subtraction of background" tool in a "sliding paraboloid" option. After enhancing the contrasted images by the contrast-limited adaptive histogram equalization, the background of images was removed using the function of "mathematical and exponential". The images were binarized using the "threshold" command, and the quantified number and area of vinculin-stained FA particles were obtained using the "analyze particles" command.

2.3.8. Flow Cytometric Analysis. PDLF and BMMSC at the third passage were incubated on scaffolds or TCP in growth medium. At 5 days post incubation, cells were processed for fixation and permeabilization using a fixation/permeabilization solution and perm/wash buffer (BD Biosciences). After washing, cells were stained with an MSC-specific surface marker, CD105, in combination with and without anti-YAP and anti-OPN antibodies. Cell populations positively expressing YAP, OPN, CD105, or all of them were analyzed using a multicolor flow cytometer (BD Biosciences) and FlowJo software.

2.3.9. Proliferation and Differentiation Assays. Cell proliferation rate was determined using Cell Counting Kit-8 (CCK-8; Dojindo Molecular Tech., Kumamoto, Japan) following the manufacturer's instructions. The optical density specific to the yellow-colored formazan was determined at 450 nm using a microplate reader (SPECTROstar Nano, BMG LABTECH, Ortenberg, Germany). Osteogenic differentiation of PDLF was determined by Alizarin Red S (ARS) staining after incubation in osteogenic medium (DMEM supplemented with 5% of FBS, 100 nM of **d**examethasone, 50 μM of **a**scorbic acid, and 10 mM of β-**g**lycerophosphate (DAG)). The potential of PDLF to stimulate osteoclastic differentiation was determined using a combined culture system with bone marrow monocytes (BMM), as described previously.[26] Here, RPMI-1640 medium supplemented with 100 nM of **d**examethasone and 10 nM of **v**itamin **D_3** (DVD) was used as the osteoclastogenic medium. Osteoclast formation was determined by tartrate-resistant acid phosphatase (TRAP) staining using a leukocyte acid phosphatase kit (COSMO BIO CO., LTD, Tokyo, Japan). The detailed methods for these assays are described in the Supporting Information.

2.3.10. si-YAP Transfection Assay. PDLFs were transfected with YAP-specific small interfering (si) or nonspecific si-control RNAs (Santa Cruz Biotechnology) according to the manufacturer's instructions. At 5 days post transfection, the proliferation rate of the cells was determined by measuring the CCK-8 dye-specific optical density at 450 nm. The impact of si-YAP on the mineralization of PDLF was analyzed by measuring the ARS-specific optical density at 14 days post incubation in osteogenic medium. The si-RNA-transfected PDLFs were also immunostained with anti-OPN and its specific secondary antibodies at 5 days post incubation. The OPN-specific intensity (a.u.) and morphological characteristics such as roundness, aspect ratio, and circularity were determined by CLSM.

2.4. Construction of Fiber−Hydrogel Complex (FHGC) and Assays for PDL Regeneration. *2.4.1. Fabrication and Characterization of FHGC.* Briefly, each of the scaffolds was cross-linked with a decalcified ECM-mimic SIS gel and exposed to UV light for 6 min at

https://doi.org/10.1021/acsami.2c18893
ACS Appl. Mater. Interfaces 2023, 15, 599−616

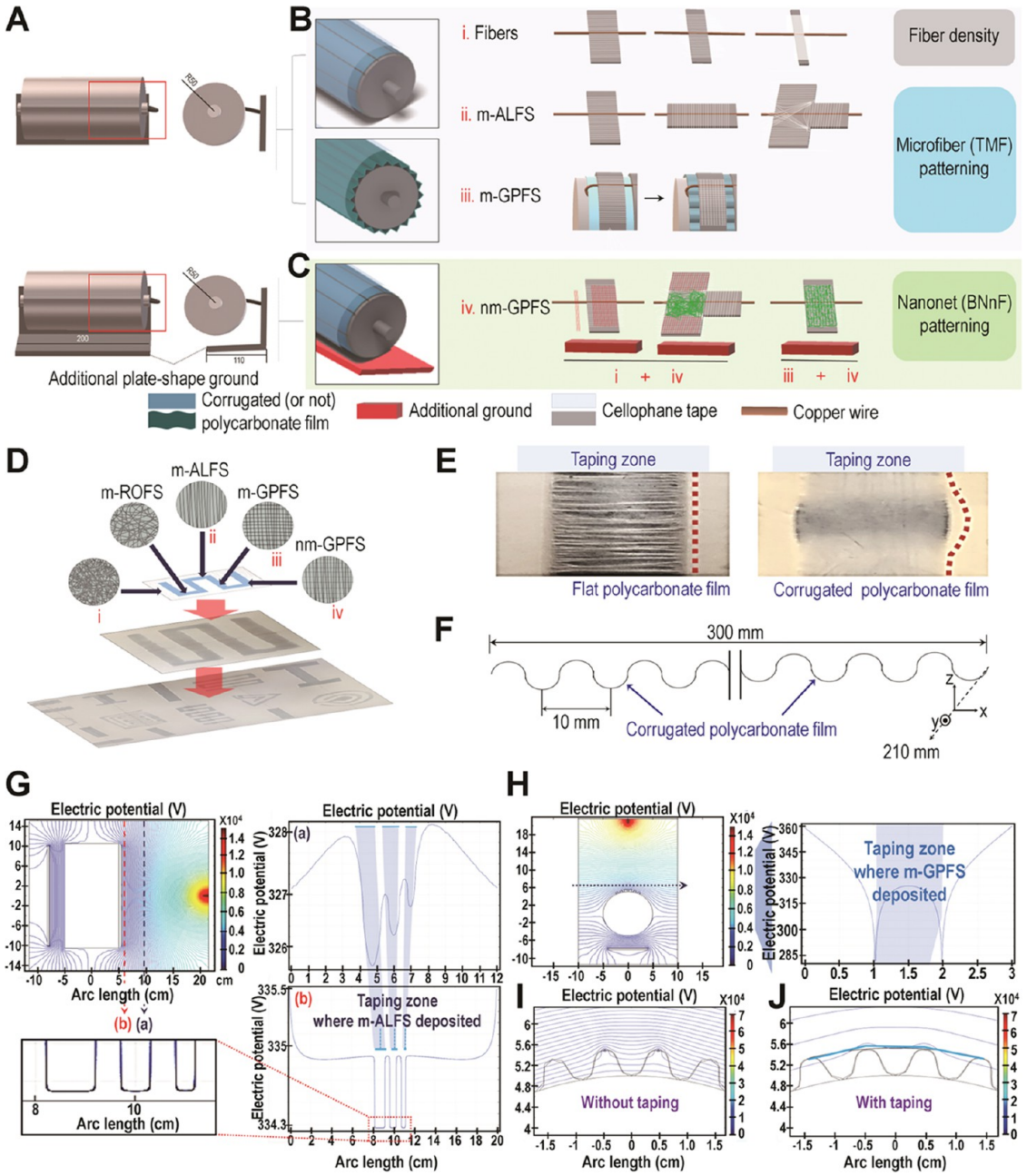

Figure 1. All-in-one electrospinning and electric field distribution for optimized fiber patterning. (A) Illustration of the optimized setup of the ground that is different for each fiber pattern. (B) Illustration of the collector modified to copper wire, cellophane tape, and corrugated (or not) polycarbonate film. (C) Additional ground installed for additional nanonet patterning from microfibers. (D) A schematic illustration of the all-in-one electrospinning that allows complete control and simultaneous patterning of microfibers or in combination with nanonets on a desired single mat. (E) Digital photograph of the alignment fibers on tape and grid-patterned fibers between the corrugated pitches (from crest to crest), where the red dot lines of the images highlight the morphology of the polycarbonate film. (F) Illustration of the detailed information of the corrugated polycarbonate sheet under bending attached to the rotating collector. (G) Electric field distribution in infinity domains and electrical potential graphs of the magnified part formed on cellophane tapes along different *xz*-cutting planes or (H) on corrugated pitch and crest-top of corrugation of the polycarbonate film. The magnified part of the electric field distribution in infinity domains formed on a corrugated polycarbonate film (I) without or (J) with tape.

365 nm. The scaffold-SIS gels were cut into a thickness of 300 μm perpendicular to the direction of scaffolds, and covered with BMP2 gels. After exposure to UV light for 1 min, the fiber−hydrogel complexes, FHGCs, were cut into a circle form (1 mm diameter × 1 mm depth) and kept at 4 °C until use. SIS and BMP2 gel complex (GC) without a linking with scaffold were used as the material comparative to FHGC. The FHGC was characterized using a Fourier transform infrared (FTIR) spectrometer (Bomen, Canada), XRD, and universal testing machine (MTDI Inc., Seoul, South Korea). Detailed methods for the characterization are provided in the Supporting Information.

2.4.2. Creation of PDL Defect and Implantation with GC or FHGC. The male rats (7 weeks old) received a general anesthesia via the intramuscular injection of Rompun (10 mg/kg; Bayer Korea Ltd., Seoul, South Korea) and Zoletil (0.4 mL/kg; Virbac Laboratories, Carros, France). Operation region was treated with 10% betadine (Sam Li Korea, Seoul, South Korea), and gingiva was carefully excised from the periodontium. Circular defect (1 mm diameter × 1 mm length) of the PDL including a portion of alveolar bone was created in the maxillary region using a trephine bur (TB-4, MCT Bio., Seongnam, South Korea). Defected regions were implanted with FHGC or GC,

https://doi.org/10.1021/acsami.2c18893
ACS Appl. Mater. Interfaces 2023, 15, 599−616

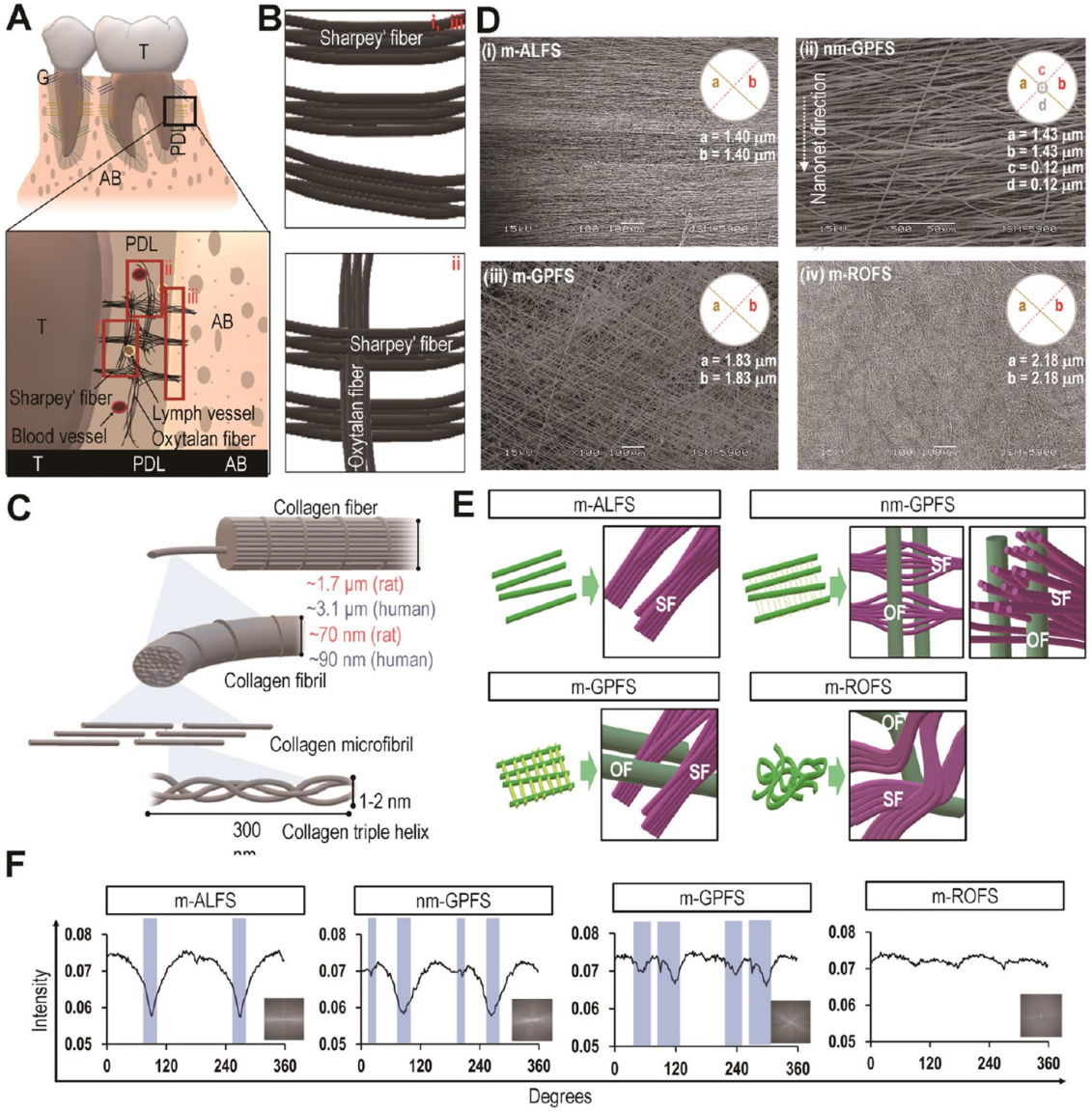

Figure 2. As-spun scaffolds mimic the oriented structure and diameter of native PDL fibers. (A) Composition of the periodontium (upper panel) and structure and location of the PDL fibers including lymph and blood vessels (below panel). (B) Illustrations exhibiting the structure of the Sharpey fibers and a cross-linked form with oxytalan fibers. (C) Illustrations describing the average diameters of PDL fibers and fibrils present in rats and humans. (D) SEM images showing the morphologies of aligned, grid/patterned, and randomly oriented fibrous scaffolds, where the scaffold-specific diameters of microfibers (a and b) and nanonets (c and d) are shown. Bar = 100 μm in m-ALFS, m-GPFS, and m-ROFS, or 50 μm in nm-GPFS. (E) Schematic diagrams showing that the morphology and structure of the as-spun scaffolds mimic that of Sharpey's and/or oxytalan fibers present in the PDL. (F) The plots of frequency and 2D FFT output images for the representative SEM images of each scaffold. AB, alveolar bone; G, gingiva; T, tooth; SF, Sharpey's fiber; OF, oxytalan fiber.

and surgical sites were sutured with 6−0 chromic gut internally and 4-0 silk externally. Postoperative prophylaxis was performed by the intramuscular injection of Amikacin (20 mg/mL) at a dose of 0.15 mL/kg of body weight for 3 days. In this assay, rats that received surgical defect only were used as the sham group.

2.4.3. Evaluation of FHGC-Induced PDL Reparation. Periodontal tissue samples including defected regions were obtained at 8 weeks post surgery, fixed in 4% paraformaldehyde, and decalcified in 17% EDTA for 3 weeks. The samples were dehydrated with a graded series of ethanol (70, 80, 90, and 100%), embedded with paraffin, and sectioned horizontally to the tooth and alveolar bone into a thickness of 7 μm. The sectioned samples were stained with hematoxylin and eosin (H&E), and the thickness of the reformed PDL was calculated at two regions that are vertical to the tooth. To examine whether there is a relationship between PDL regeneration and alveolar bone healing, the value of alveolar bone volume (BV; mm^3) in defected regions was evaluated by microcomputed tomography (μCT). Expression of YAP in the reformed PDL was analyzed by immunohistochemistry (IHC) using anti-YAP antibody and mouse-anti-Vectastain ABC DAB-HRP kit (Vector Laboratories, Burlingame, CA) following the manufacturer's instructions. Based on the IHC results, the expression pattern of YAP and number of PDL cells exhibiting a round-shaped or fiber-oriented elongation were evaluated. Levels of YAP and OPN in the reformed PDL were also determined by CLSM after immunofluorescence staining. In addition, fiber patterning and diameter (nm) in the reformed PDL of the animal groups were analyzed by TEM.

2.5. Statistical Analyses. All data are represented as the mean ± standard deviation (SD) and analyzed using SPSS version 16.0 software. Differences between two groups were analyzed by unpaired Student's *t*-test. One-way analysis of variance (ANOVA) followed by a post hoc Tukey test was used for multiple comparisons among more

https://doi.org/10.1021/acsami.2c18893
ACS Appl. Mater. Interfaces 2023, 15, 599−616

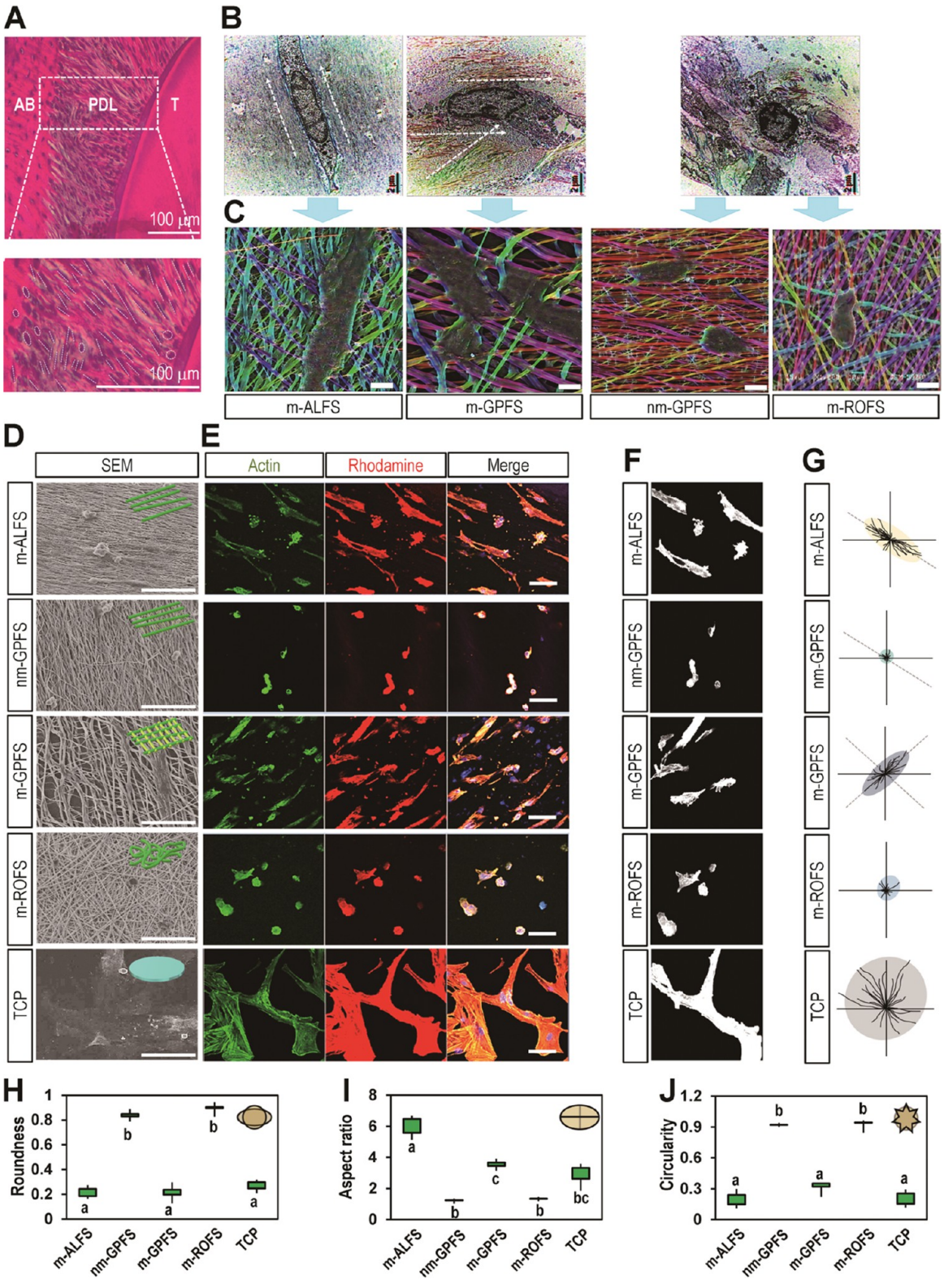

Figure 3. Scaffold-seeded PDLFs exhibit fiber-specific morphologies similar to the cells present in the PDL. (A) H&E-stained images of rat periodontium, where the fiber-oriented (white dotted lines) and round-shaped PDL cells (white dotted circles) are indicated (below panel). (B) TEM images showing the fiber-dependent elongated or round-shaped cells in rat PDL. Bar = 2 μm. (C) False color-coded SEM images showing the morphological peculiarity of PDLF grown on the as-spun scaffolds. Bar = 0.5 μm. Fiber topography-dependent elongation and round-shaped morphologies in cultured PDLF are shown by (D) TEM and (E) CLSM after staining with actin (green) and RP-F-actin (red). Bar = 50 μm. Illustrations describing the cytoskeletal directionality, length, and spreading size of scaffold- or TCP-seeded PDLF using (F) ImageJ and (G) NeuronJ plugin. (H) Roundness, (I) aspect ratio, and (J) circularity of PDLF grown on the as-spun scaffolds or TCP. The superscripts$^{(a-c)}$ represent a significant difference at $p < 0.05$ among the groups by ANOVA ($n = 5$).

https://doi.org/10.1021/acsami.2c18893
ACS Appl. Mater. Interfaces 2023, 15, 599−616

than two groups. A value of $p < 0.05$ was considered statistically significant.

3. RESULTS

3.1. All-In-One Electrospinning and Electric Field Simulations. Figure 1A shows an additional plate-shaped ground plane that is installed under the current collector to achieve the simultaneous patterning of nanonets and microfibers. Detailed information regarding the design of an optimized setup for nanonet patterning with additional ground in the fabrication of nm-GPFS is provided in Figure S3A,B. Digital images of collector modification for the fabrication of m-ALFS and m-GPFS are also shown in Figure S3C. When several copper-enameled wires were attached to the polycarbonate film at intervals of 3−8 cm in combination with the cellophane tape, an increased density of fibers along with a decreased diameter of the cellophane tape was obtained in aligned fibrous scaffold (Figure 1B-i). The direction of the cellophane tape to copper-enameled wires determined fiber orientation in the m-ALFS (Figure 1B-ii). Corrugated polycarbonate films and additional plate-type ground were also applied to develop engineered fibrillar microenvironments with a controllable architecture. In this regard, the attachment of the corrugated polycarbonate film under the rotor-attached bending instead of a flat film allowed a grid-patterning in the m-GPFS (Figure 1B-iii). The installation of an additional plate-shaped ground plane under the current collector also provided an optimized setup to simultaneously pattern nanonets from microfibers in the nm-GPFS (Figure 1C-iv). We found that nanonets in the nm-GPFS were mainly filled in an orthogonal direction across the aligned and radial fibers (red lines, i + iv), whereas the nanonets between the lattice and random pattern fibers (green lines, iii + iv) were irregularly filled. The illustration and digital photographs in Figure 1D show various fiber patterning fabricated on a desired single mat via one or more application of the modified methods. The digital photographs in Figure 1E indicate the taping zone of patterned fibers deposited with a flat or corrugated polycarbonate film. Morphological information of a corrugated polycarbonate film under a bending attached to the rotor is also shown in Figure 1F.

As an electric field is the major driving force to control the pattern and density of fibers, we performed electric field simulations using the COMSOL program with the AC/DC module. Based on the electrical potential graph, an apparent difference between the edge of cellophane tape where electric charges had been accumulated by the copper wire and other part of cellophane tape was found (Figure 1G). In contrast, such a difference between the periphery and the tape tended to be varied depending on the thickness of the tape (Figure 1G-a). The difference induced by the tape thickness allowed different densities of aligned nanofibers. Copper wires supplied a constant electric charge to the cellophane tape to uniformly deposit the fibers aligned into a uniaxial array on the cellophane tape (Figure 1G-b). Figure 1H exhibits a change of charge accumulated in the crest-top of corrugation that is applied to fabricate grid-patterned fibers. This figure not only indicates the crest-tops of the corrugations that act as parallel electrodes, thereby forming a uniaxially aligned array, but also shows sharp peaks at the crest-tops of the corrugations. We also found that the electric field between the corrugated pitches was formed with an appropriate strength in an orthogonal direction to the electric field formed by the copper wire and the tape, as well as with the fiber patterning in an orthogonal shape (Figure 1I,J). Furthermore, this study highlights the advantages of the developed electrospinning in the formation of patterned nanonets (Figure S4A−D). All of these data demonstrate that the developed electrospinning setup overcomes the limitations derived from the parallel electrode setup by transferring the residual charge that causes a strong electric repulsion acting between adjacent fibers across the air gap into the cellophane membrane.

3.2. Native PDL Matrix-Mimetic Structure, Orientation, and Diameter of the As-Spun Scaffolds. Figure S5 illustrates the location, orientation, and structural and morphological phenotypes of Sharpey's and oxytalan fibers in rat and/or human PDL samples. These SEM and TEM images indicated that the PDL fibrous matrix consisted mainly of Sharpey's and oxytalan fibers with an aligned or cross-linked form (Figure 2A,B). Considering the SEM and TEM images, the mean diameters of bundled PDL collagen fibers and fibrils were estimated as ∼1.7 μm and ∼70 nm in rats and ∼3.1 μm and ∼90 nm in humans, respectively (Figure 2C). SEM images exhibited a characteristic patterning or random-orientation corresponding to each of the as-spun scaffolds, where the average diameters of microscale and nanonet fibers in the scaffolds were 1.71 and 0.12 μm, respectively (Figure 2D). These images also indicated that the structure of the m-ALFS mimics that of Sharpey's fibers (Figure 2D-i,E), while that of m-GPFS exhibits its cross-linked structure with oxytalan fibers (Figure 2D-iii,E). The nm-GPFS showed a PDL fibrous structure composed of PDL-mimicking microfibers and nanonet-patterned fibers (Figure 2D-ii,E). However, it is considered that the structure of m-ROFS is different from that present in native PDL, even though it may express a microscale structure corresponding to Sharpey's and/or oxytalan fibers (Figure 2D-iv,E). To further investigate the fiber orientation, the representative SEM images of each scaffold were converted to frequency plot and 2D FFT output images, presenting as grayscale pixels (Figure 2F). As shown in the figure, the m-ROFS showed apparently different properties compared with that of other fibrous scaffolds, in which the m-GPFS revealed a relatively broad distribution of the microfiber angle (blue box) than did m-ALFS or nm-GPFS.

3.3. Fiber Topography-Dependent Morphological Phenotypes of PDLFs. Morphology, behavior, and the function of PDLF could be tightly affected by their location within the PDL, as well as by the structure of the surrounding fibers such as Sharpey's and oxytalan fibers. We monitored how PDLFs exhibit their morphological phenotypes in the intact PDL and whether their morphologies are altered depending on the structure of PDL fibers. The results from the H&E staining of rat PDL revealed that PDLFs are mostly oriented along the fibers together with a few round-shaped cells near the cementum and alveolar bone (Figure 3A). TEM images clarified the presence of fiber-oriented and round-shaped cells in a rat PDL sample (Figure 3B). False color coding in SEM images supported the fiber surface-dependent morphology of PDLF, in which m-ALFS- and m-GPFS-seeded cells exhibited an elongated and fiber-oriented morphology, whereas nm-GPFS and m-ROFS are predominantly small and round-shaped (Figure 3C). The fiber topography-related alteration in morphology and cytoskeletal organization was also observed in the cultured PDLF by SEM (Figure 3D). Similarly, CLSM images revealed that almost all PDLFs grown on m-ALFS and m-GPFS expressed fiber-oriented and elongated cytoskeletal organization, but approximately 90% of the cells on nm-GPFS and m-ROFS exhibited a round morphology (Figure 3E). The evaluation of fluorescence intensity specific to F-actin using

https://doi.org/10.1021/acsami.2c18893
ACS Appl. Mater. Interfaces 2023, 15, 599−616

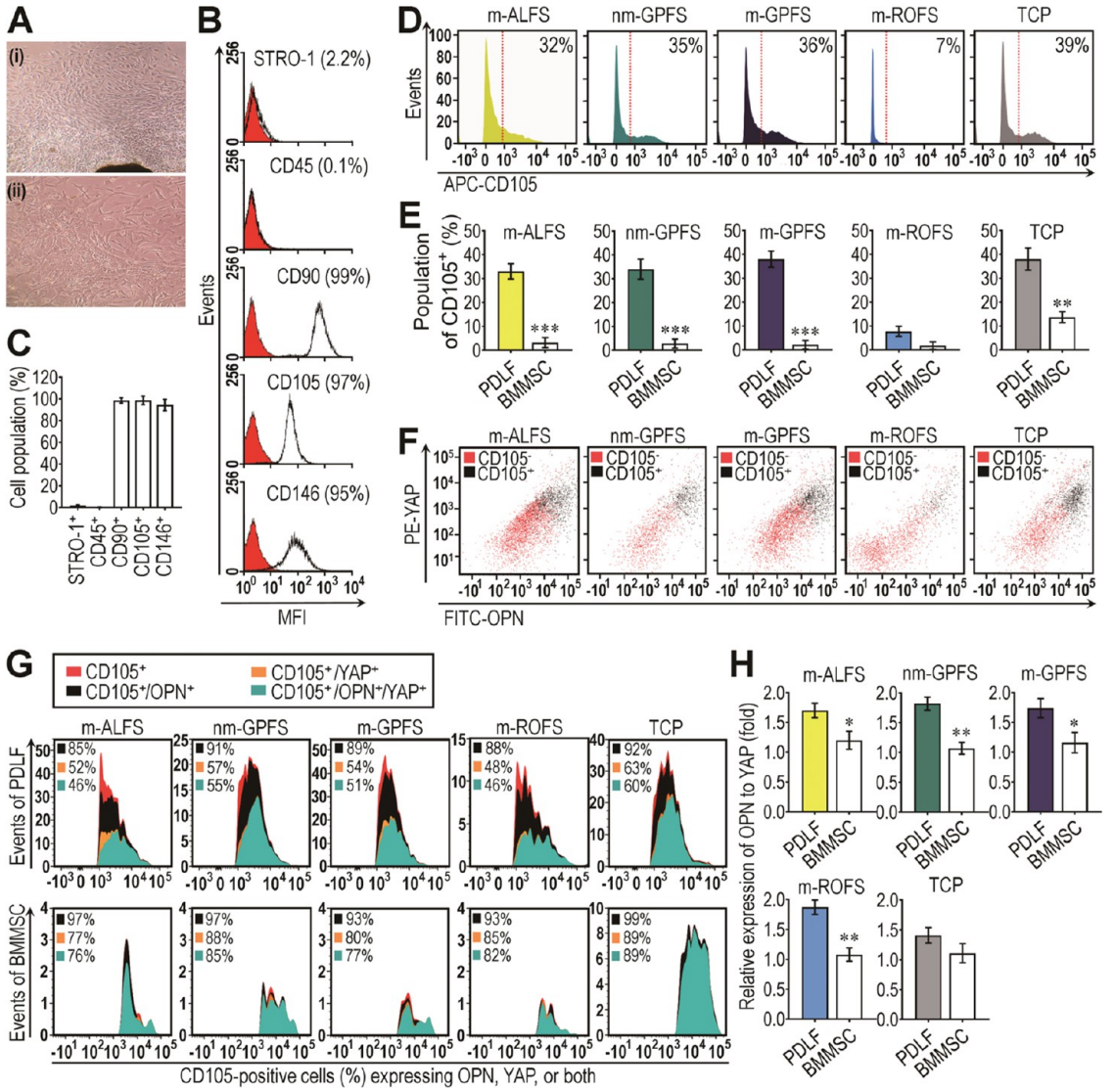

Figure 4. Expression of MSC-specific surface markers and mechanosensing molecules in PDLF differed from that in BMMSC. (A) Morphological observation of PDLF at (i) the first and (ii) the third passages by optic microscopy. (B) Populations expressing the indicated surface markers in PDLF at the first passage. (C) The mean population (%) of PDLF expressing each of the surface markers ($n = 3$). (D) Level of CD105-positive PDLF at the third passage. (E) Numbers of CD105-positive PDLF and BMMSC at the third passage ($n = 3$). (F) The correlated expression patterns between CD105 and YAP or OPN in the PDLF cultures at the third passage. (G) The population (%) of cells expressing YAP, OPN, or both in CD105-positive PDLF and BMMSC. (H) Relative expression of OPN to that of YAP in PDLF and BMMSC ($n = 4$). PDLFs in panels A−C were cultured on TCP, whereas the cells in panels D−H were on the indicated fibrous scaffolds or TCP. *$p < 0.05$, **$p < 0.01$, and ***$p < 0.001$ vs the values in PDLF by unpaired Student's *t*-test.

ImageJ (Figure 3F) and NeuronJ plugin (Figure 3G) also supported fiber surface-dependent morphological alterations in cultured PDLF. In addition, the PDLF grown on nm-GPFS or m-ROFS showed greater roundness (Figure 3H) and circularity (Figure 3J) compared with those grown on m-ALFS or m-GPFS, whereas the aspect ratio (Figure 3I) of the cells on m-ALFS and m-GPFS was significantly higher than that on nm-GPFS and m-ROFS. The PDLF grown on TCP revealed similar values of roundness, aspect ratio, and circularity to that of m-ALFS- or m-GPFS-seeded cells despite their cytoskeletal spreading greater than that on the scaffolds.

3.4. Characterization of Cell Surface Markers in PDLF and Their Relationship with the Expression of CD105, YAP, and OPN. PDL contains various types of cells together with a few PDLSCs. We determined the expression patterns of several MSC-associated surface markers in PDLF and investigated how the as-spun scaffolds alter the expression of surface markers by flow cytometric analysis. The PDLF grown on TCP exhibited fibroblast-specific morphology both at the first (Figure 4A-i) and the third passages (Figure 4A-ii), whereas a proportion of the cells showed a clonogenic morphology only at the first passage. Similar to previous findings,[14] CD90, CD105, and CD146, but not CD45, were highly expressed in almost all of the PDLFs cultured on TCP at the first passage, whereas approximately 2% expressed STRO-1, a PDLSC-specific surface marker (Figure 4B,C). Compared with the first passage, all PDLF cultures showed a marked reduction in CD105 at the third passage after 5 days of incubation, regardless of cultures on the fibrous scaffold or TCP (Figure 4D). Among the cultures, the PDLF incubated on m-ROFS exhibited the lowest level of CD105-expressing cells. Interestingly, however, the PDLF incubated on m-ALFS, nm-GPFS, m-GPFS, or TCP,

https://doi.org/10.1021/acsami.2c18893
ACS Appl. Mater. Interfaces 2023, 15, 599−616

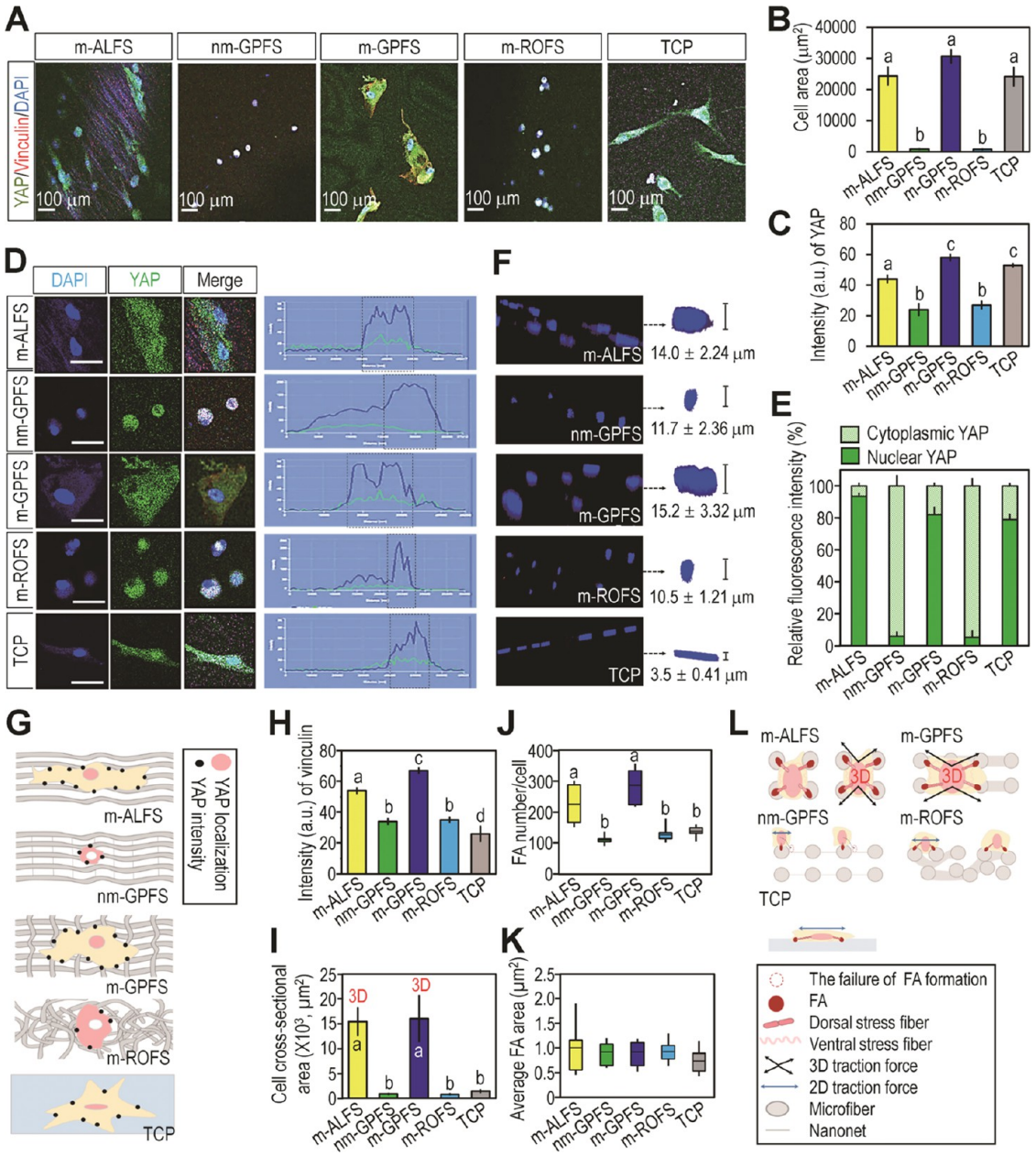

Figure 5. Fiber topography-regulated morphological phenotypes in cultured PDLF are correlated with the expression of mechanosensing molecules and FA formation. (A) The merged CLSM images showing the expression pattern and cellular location of YAP (green) and vinculin (red) in PDLF at 5 days post incubation. Bar = 100 μm. (B) The area of PDLF (n = 5) and (C) the mean fluorescence intensity (a.u.) specific to YAP (n = 5). (D) CLSM images exhibiting the expression and cellular localization of YAP in cultured PDLF at 5 days post incubation. Bar = 50 μm. (E) The relative fluorescence intensity (%) of cytoplasmic and nuclear YAP in cultured PDLF (n = 5). (F) The orthogonal and cross-sectional z-stack nuclear morphology together with the mean nuclear thickness (μm) in cultured PDLF. (G) Schematic diagrams representing the fiber surface-dependent intensity and localization of YAP along with traction force in cultured PDLF. (H) The mean fluorescence intensity (a.u.) specific to vinculin (n = 5). (I) Cell cross-sectional area (n = 5). (J) Number of FA per cell (n = 5). (K) Average FA area (n = 5). (L) Schematic diagram showing the relationship between surface-dependent FA formation and cell traction force (2D or 3D) for scaffolds composed of nanonets and microfibers. The superscripts$^{(a-d)}$ represent a significant difference at $p < 0.05$ among the groups by ANOVA (n = 5).

but not on m-ROFS, revealed significantly higher numbers of CD105-expressing cells compared with BMMSC at the same passage and incubation time (Figure 4E). Dissimilar to BMMSC (Figure S6), the cultured PDLF also indicated that the expression of CD105 is entirely proportional to that of YAP and OPN regardless of the incubation on scaffolds or TCP (Figure 4F). We further analyzed the pattern of PDLF expressing YAP, OPN, or both in the CD105-positive cells by gating the marker-expressing cells. Both PDLF and BMMSC showed greater expression of OPN compared with that of YAP, whereas the numbers of cells expressing both YAP and OPN were higher in BMMSC than in PDLF (Figure 4G). A significantly greater level of OPN to that of YAP was determined in CD105-expressing cells in PDLF cultured on scaffolds, but not on TCP, than in BMMSC (Figure 4H). These results indicate that the expression of YAP in PDLF is correlated with that of OPN and CD105, and this is affected differently in relation to the fiber topographies of scaffolds.

https://doi.org/10.1021/acsami.2c18893
ACS Appl. Mater. Interfaces 2023, 15, 599−616

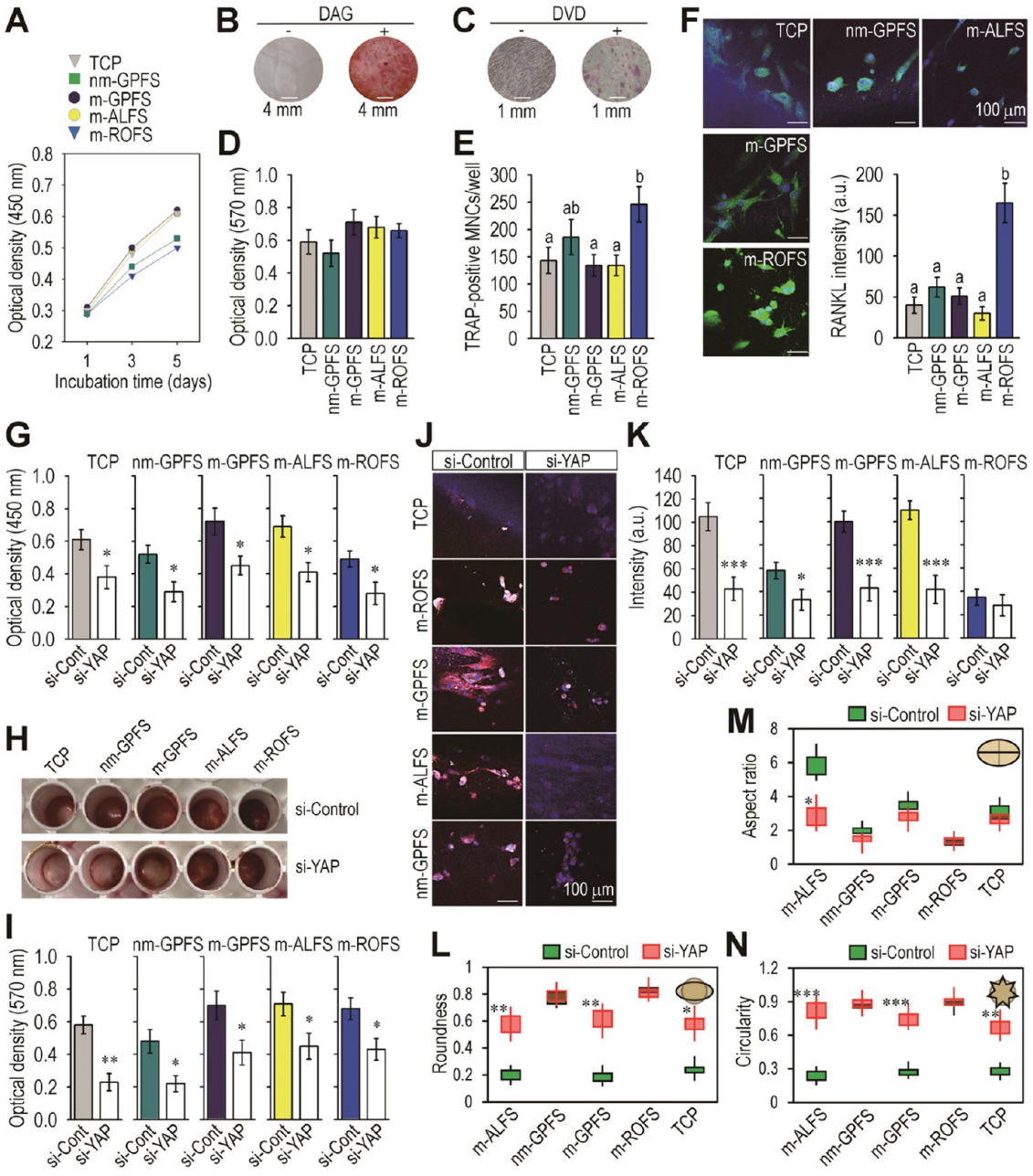

Figure 6. PDLF exerts different proliferating and differentiating potentials in relation to the fiber topographical cues of scaffolds, as well as via the regulation of YAP-mediated signaling. (A) CCK-8 dye-specific optical density in PDLF incubated for 1, 3, or 5 days. (B) ARS staining showing the DAG-mediated mineralization of PDLF. (C) TRAP staining exhibiting the formation of multinucleated cells (MNCs) in combined cultures with PDLF and BMM. (D) The mean optical density specific to ARS dye ($n = 3$) in the PDLF cultures and (E) the number of TRAP-positive MNCs/well ($n = 5$) in the combined cultures with BMM. (F) CLSM images showing the expression of RANKL (green) in cultured PDLF (Bar = 100 μm) and its mean fluorescence intensity (a.u.) ($n = 5$). (G) The mean optical density specific to CCK-8 dye in si-control and si-YAP transfected PDLF at 5 days post incubation ($n = 5$). (H) ARS staining showing the mineralization in the transfected PDLF. (I) The mean optical density specific to ARS dye in the transfected PDLF ($n = 5$). (J) CLSM images showing OPN expression in the cells. (K) The mean fluorescence intensity (a.u.) of OPN in the PDLF cultures ($n = 5$). (L) Roundness, (M) aspect ratio, and (N) circularity in the transfected PDLF ($n = 5$). The superscripts[(a and b)] represent a significant difference at $p < 0.05$ among the groups by ANOVA ($n = 5$). *$p < 0.05$, **$p < 0.01$, and ***$p < 0.001$ vs the si-control PDLF by unpaired Student's t-test.

3.5. Correlation of FA Formation and YAP Expression and Localization with the Area and Dimension of Scaffold-Seeded PDLF. We subsequently investigated whether there is a relationship between the expression and intensity of YAP and FA formation with morphological alterations of scaffold-seeded PDLF. The merged CLSM images from immunofluorescence staining showed that cultured PDLFs express vinculin, OPN, COLI, and YAP in relation to the fiber topographic cues (Figures 5A and S7A). The area (μm^2) of cultured PDLF was closely associated with the intensity (a.u.) of YAP, where the cells grown on m-ALFS or m-GPFS revealed greater cell area than did the nm-GPFS or m-ROFS (Figure 5B,C). The calculation of fluorescence intensity specific to OPN and COL1 also indicated the correlation of OPN with the fiber topographic-related morphology of PDLF (Figure S7B). We next evaluated the expression intensity of YAP and its nuclear-

https://doi.org/10.1021/acsami.2c18893
ACS Appl. Mater. Interfaces 2023, 15, 599−616

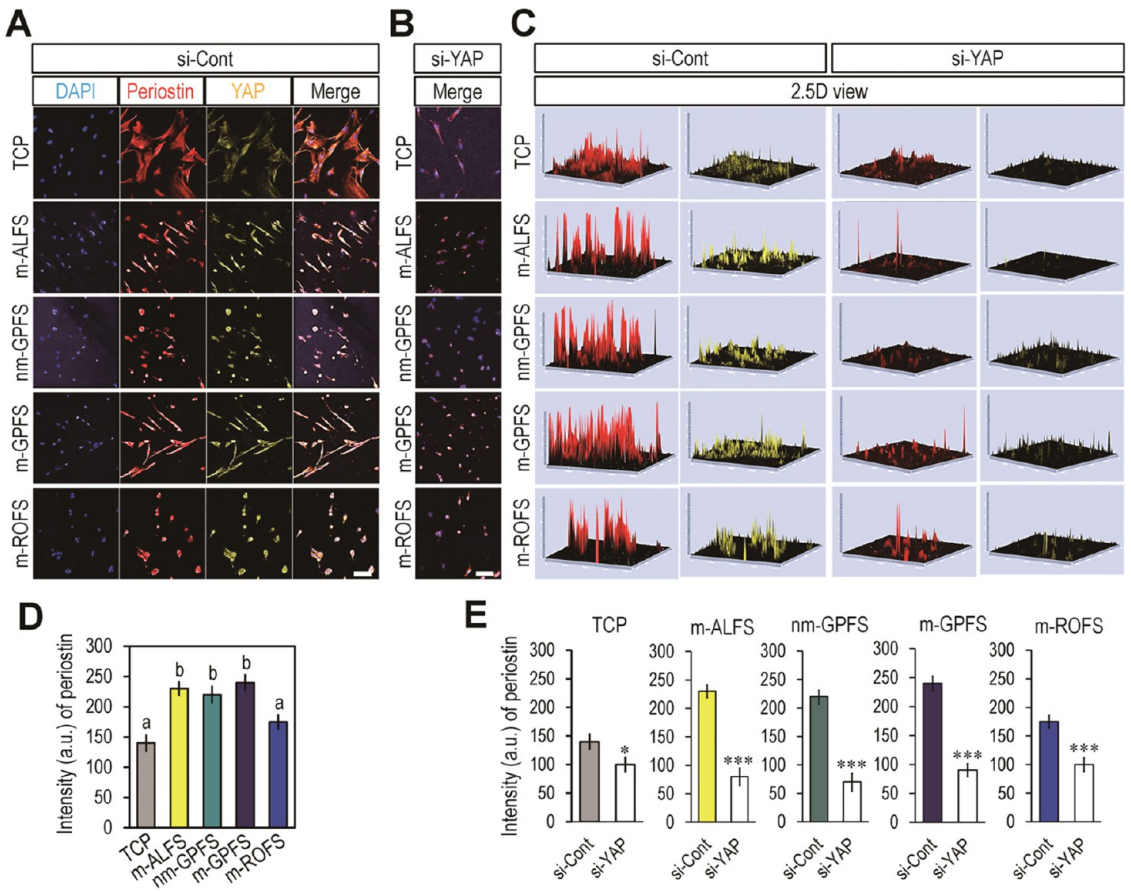

Figure 7. YAP-mediated signaling modulates periostin, a PDL essential marker for periodontal tissue remodeling. CLSM images showing the expression of periostin (red) and YAP (yellow) in the PDLF transfected with (A) si-control or (B) si-YAP at 5 days post incubation ($n = 5$). Bar = 100 μm. (C) CLSM images were converted into 2.5D (pseudo 3D) images, by which the fiber topography-associated signals specific to YAP (yellow) and periostin (red) were provided. (D) The mean fluorescence intensity (a.u.) specific to periostin ($n = 5$). (E) The mean fluorescence intensity (a.u.) of periostin in the PDLF transfected with si-control or si-YAP at 5 days post incubation ($n = 5$). The superscripts[a and b] represent a significant difference at $p < 0.05$ among the groups by ANOVA ($n = 5$). *$p < 0.05$ and ***$p < 0.001$ vs the si-control PDLF by unpaired Student's t-test.

cytoplasmic shuttling by using CLSM. The expression pattern of YAP along with cellular morphology differed in relation to the fiber topographies of scaffolds (Figure 5D). The PDLF grown on m-ALFS or m-GPFS showed YAP-specific intensity in the nucleus more greatly than in the cytoplasm compared with the cells seeded on nm-GPFS or m-ROFS (Figure 5E). Similarly, the nuclear shape remodeling via z-stacked 3D construction represented greater nuclear thickness in the PDLF grown on m-ALFS or m-GPFS compared with that grown on nm-GPFS or m-ROFS (Figure 5F). These results indicate that the intensity and localization of YAP in cultured PDLF are tightly affected depending on the fiber topographies of scaffolds, where m-ALFS and m-GPFS exhibit higher YAP expression than do other scaffolds (Figure 5G). Our results also postulate a closed relationship between the expression and nuclear localization of YAP and the spreading and nuclear thickness of PDLF. While the traction force may induce the nuclear localization of YAP, FAs modulate the force transfer by mediating external or internal responses derived from the cytoskeletal network. Vinculin is one of the major components of FAs and regulates cell shape, area, and traction force. Thus, we further evaluated the relationship between FA formation and traction force based on the CLSM images of vinculin/YAP-double-stained PDLF. Both m-ALFS and m-GPFS exhibited greater values in the intensity of vinculin (Figure 5H), 3D cell cross-sectional area (Figure 5I), and FA numbers (Figure 5J), although the average FA area did not differ among the groups (Figure 5K). Similar to the result shown in Figure 5I, SEM images indicated fiber topography-dependent 3D cell morphology and spreading of PDLF (Figure S8). Based on the SEM images, we analyzed the number and area of 3D-generated FA using the Z-stack technique in the programs of ImageJ and ZEN. Figure 5L shows a schematic diagram that supports the apparent FA formation and cell spreading of PDLF grown on m-GPFS or m-ALFS. Taken together, our results indicate a close association between morphological phenotypes and YAP expression, traction force, and/or FA formation in relation to the fiber topographies of scaffolds.

3.6. Fiber Topography-Associated and YAP-Regulated Proliferation and Differentiation of PDLF. We evaluated the fiber topography-associated impacts of scaffolds on PDLF proliferation by CCK-8 assay. We also examined the effects of scaffolds on the osteogenic differentiation of PDLF by ARS staining, as well as on osteoclastic activation by TRAP staining. In these assays, the PDLFs incubated on TCP were used as a comparative control group. In TRAP staining assay, PDLFs were used as mechanosensitive and osteoclastogenic feeder cells in the combined culture with BMM. Similar to that in TCP-seeded PDLF, the growth rate of scaffold-seeded cells was in an incubation time-dependent manner, and m-ALFS and m-GPFS stimulated PDLF proliferation more greatly than nm-GPFS and

https://doi.org/10.1021/acsami.2c18893
ACS Appl. Mater. Interfaces 2023, 15, 599−616

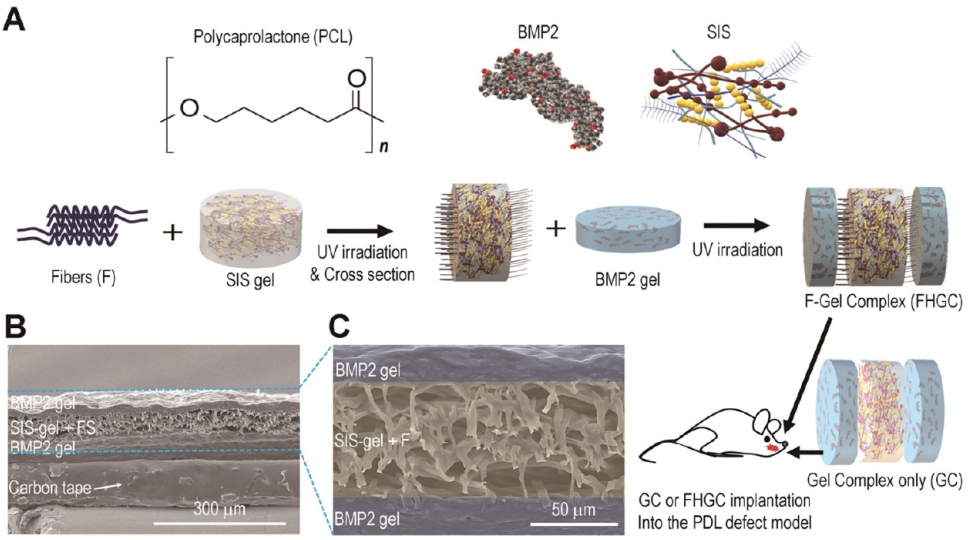

Figure 8. Schematic illustrations to fabricate GC and FHGC and their SEM images. (A) Schematic illustrations showing the structure of materials and the procedures to fabricate FHGC before implantation. SEM images representing (B) a broad space of cross-sectioned FHGC (bar = 100 μm) and (C) the location of fibers and gels in FHGC.

m-ROFS (Figure 6A). When PDLFs were incubated on TCP in medium containing DAG or DAG-free medium for 14 days, a marked mineralization was found only in the DAG-treated culture (Figure 6B). The cultured PDLF in combination with BMM for 7 days in the presence of DVD induced the formation of multinucleated osteoclasts (Figure 6C). The PDLF cultured on scaffolds in DAG-supplemented medium for 14 days showed ARS dye-specific optical density similar to that of TCP-seeded cells (Figure 6D). However, the number of TRAP-positive multinucleated cells was significantly higher in the combined cultures on m-ROFS compared with that on TCP, m-GPFS, or m-ALFS (Figure 6E). Similarly, immunofluorescence staining of the PDLF incubated in DVD-supplemented medium for 5 days showed that the m-ROFS-seeded PDLF expressed the highest RANKL-specific intensity (a.u.) among the control and experimental groups (Figure 6F). To understand the regulatory roles of YAP on PDLF behavior, we knocked down the expression of YAP in PDLF by si-RNA transfection and evaluated the si-YAP impacts on proliferation, mineralization, OPN expression, and morphological alteration. All cultures of si-YAP-transfected PDLF on scaffolds or TCP showed a significantly lower proliferation rate compared with the si-control cells (Figure 6G). The si-YAP transfection diminished DAG-mediated mineralization of PDLF regardless of the cultures on scaffolds or TCP (Figure 6H,I). The expression level of OPN in the cells grown on nm-GPFS, m-GPFS, or m-ALFS, but not on m-ROFS, was significantly diminished by si-YAP transfection (Figure 6J,K). The si-YAP transfection also markedly changed the cytoskeletal morphology of PDLF depending on the fiber topography of the scaffolds, in which the roundness and circularity of the cells grown on m-ALFS, m-GPFS, or TCP were significantly augmented compared with that of the si-control cells (Figure 6L,N). In contrast, the si-YAP-mediated reduction of aspect ratio was found only in the m-ALFS-seeded PDLF (Figure 6M). These results strongly support the fiber topography-associated and YAP-mediated regulation of PDLF behaviors such as proliferation, differentiation, and morphological characteristics.

3.7. Fiber Topography-Associated and YAP-Regulated Expression of Periostin. The YAP signaling pathway plays a key role in the mechanosignal transduction. All of the current findings indicate the crucial roles of YAP in regulating fiber topography-associated behaviors of PDLF. To further verify the regulatory role of YAP on the morphology of PDLF, the fiber topography-associated expression of periostin in the PDLF transfected with si-YAP or si-control was analyzed by CLSM. Similar to the expression patterns of actin (Figure 3E), vinculin (Figure 5A), and OPN (Figure S7A), the expression of periostin was correlated with the fiber topography-associated morphological alterations of PDLF (Figure 7A). PDLFs grown on m-ALFS and m-GPFS revealed further spread and fiber-oriented morphologies compared with the cells on m-ALFS or nm-GPFS. The expression level of periostin in scaffold-seeded PDLF was transparently diminished by si-YAP transfection (Figure 7B). We subsequently converted CLSM images of periostin/YAP-double-stained PDLF into 2.5D view (pseudo 3D) and further analyzed the intensities of periostin (red color) and YAP (yellow color). Similarly, m-ALFS and m-GPFS stimulated PDLF to highly express the periostin-specific signal and its intensity compared with that of m-ROFS or TCP (Figure 7C,D). In contrast, PLDF grown on the nm-GPFS also showed periostin signal and its mean intensity similar to the cells on m-ALFS or m-GPFS. The si-YAP transfection significantly suppressed the mean intensity (a.u.) of periostin in cultured PDLF regardless of the topographies of scaffolds or TCP (Figure 7E). These results strongly support that behaviors and morphological characteristics of PDLF are tightly affected by the fiber topography of scaffolds, as well as by the YAP-associated signaling.

3.8. Fabrication of FHGC and its Physicochemical Characterization. To evaluate the potency of fibrous scaffolds on PDL reparation, we constructed a 3D-structured FHGC by conjugating each of the fibers with hydrogels. Figure 8A illustrates the structures of the PCL membrane, BMP2, and SIS gel along with the procedures to fabricate FHGC before implantation into a rat model of PDL defect. Here, we designed the integrated and patterned fiber/hydrogel biphasic scaffolds to mimic the native PDL fiber, as well as to provide an anatomical layer-by-layer structure of the periodontium. We found that approximately 52% (w/w) and 10% (v/v) of PCL membrane were contained in FHGC (data not shown). Figure 8B,C

https://doi.org/10.1021/acsami.2c18893
ACS Appl. Mater. Interfaces 2023, 15, 599−616

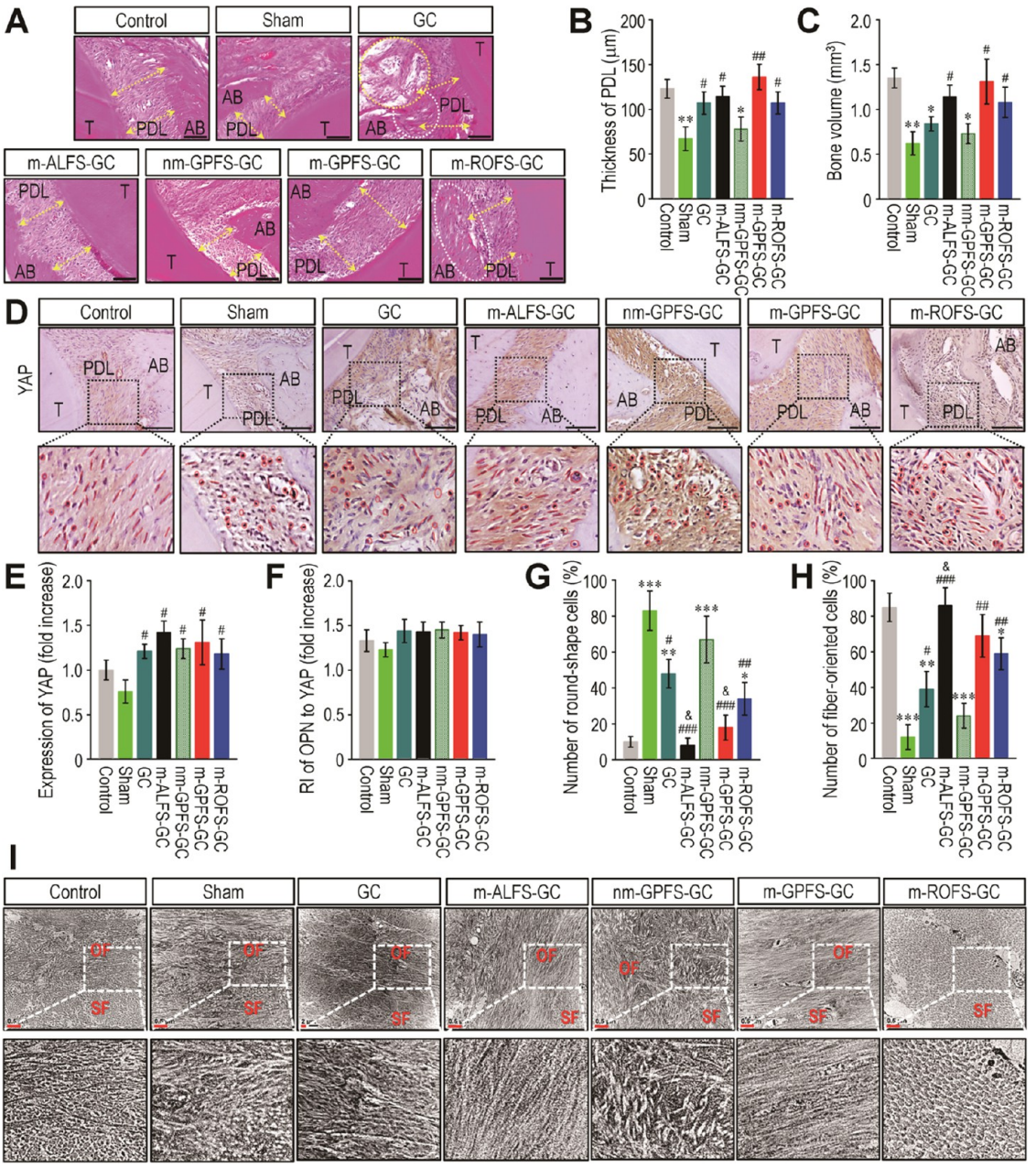

Figure 9. Implantation with m-ALFS-GC or m-GPFS-GC almost completely restores the defected PDL. (A) H&E-stained images of the defected periodontal region at 8 weeks post surgery. Yellow dotted arrows indicate the thickness of PDL, while white and yellow dotted circles show an unclear boundary between the alveolar bone and tooth and a region unfilled with tissues, respectively. Bar = 50 μm. (B) The thickness (μm) of reformed PDL (n = 5) and (C) the value of alveolar BV (mm^3) in the periodontal defect (n = 4). (D) IHC showing the expression pattern of YAP in the reformed PDL. Bar = 50 μm. (E) Expression level (fold increase) of YAP in the PDL (n = 4). (F) Relative intensity (RI) of OPN to that of YAP in the animal groups (n = 4). Numbers of (G) round-shaped and (H) fiber-oriented/elongated cells (%/100 cells/sample) in the reformed PDL (n = 4). (I) TEM images showing fiber morphology in the recovered PDL of the animal groups (bar = 0.5 μm). *p < 0.05, **p < 0.01, and ***p < 0.001 vs the control group; $^{\#}p$ < 0.05, $^{\#\#}p$ < 0.01, and $^{\#\#\#}p$ < 0.001 vs the sham group; $^{\&}$ p < 0.05 vs the GC group by unpaired Student's t-test.

represents SEM images of FHGC, showing the location and structure of fibrous scaffolds and gels. We characterized the physicochemical properties of FHGC before implantation by evaluating FTIR (Figure S9A). The crystalline structures of the PCL membrane, SIS gel, BMP2 gel, and FHGC were also investigated by XRD (Figure S9B). We evaluated the property of the hydrogel complex (GC) by analyzing its compressive property and compared it with that of FHGC linked with m-ALFS (m-ALFS-GC), nm-GPFS (nm-GPFS-GC), m-GPFS (m-GPFS-GC), or m-ROFS (m-ROFS-GC) (Figure S10A,B). We also determined contact angles (Figure S10C) and weight loss rates of FS, GC, and/or FHGC (Figure S10D).

3.9. Implantation with m-ALFS-GC or m-GPFS-GC Repairs Defected PDL More Efficiently Than GC, nm-GPFS-GC, or m-ROFS-GC. To evaluate the in vivo effect of FHGC on PDL reparation, we generated a rat model of periodontal defect and implanted the animals with GC or FHGC (Figure S11). In this experiment, rats were divided into seven groups; nonsurgical (control group), surgical operation only (sham group), surgical operation and implantation with

https://doi.org/10.1021/acsami.2c18893
ACS Appl. Mater. Interfaces 2023, 15, 599−616

GC alone (GC group), or GC linked with each of four different scaffolds (FHGC groups). At 8 weeks post surgery, PDL samples including the defective region were removed and processed for H&E staining, μCT analysis, immunofluorescence staining, and IHC. The results from H&E staining revealed a noncritical creation of the PDL defect, in that PDL reparation was found even in the sham group (Figure 9A). While the GC and m-ROFS-GC groups exhibited an unclear boundary between the alveolar bone and PDL (white dotted circles) or a large region unfilled with tissues (yellow dotted circles), the m-ALFS-GC and m-GPFS-GC groups showed an almost complete PDL reparation. When the thickness (μm) of PDL was measured at two regions (yellow dotted arrows in Figure 9A), GC, m-ALFS-GC, m-GPFS-GC, and m-ROFS-GC groups showed levels similar to that in the control group (Figure 9B). The m-ALFS-GC, m-GPFS-GC, and m-ROFS-GC groups revealed a greater level of alveolar BV (mm^3) compared with the sham group, indicating a correlation between PDL reparation and newly formed alveolar bone in the defects (Figure 9C). The IHC result did not indicate a different YAP expression between the control and the GC- or FHGC-implanted groups, whereas all of the GC or FHGC groups showed a higher YAP expression than the sham group (Figure 9D,E). Immunofluorescence assays also indicated higher intensities specific to YAP and OPN in the FHGC-implanted groups compared with those in the sham group (Figure S12). The control and FHGC-implanted groups revealed approximately 1.4-fold higher intensity of OPN compared to that of YAP without any differences among the groups (Figure 9F). Based on the magnified IHC images (Figure 9D, below panels), the proportions of round-shaped and fiber-elongated PDL cells (%) in the control group were similar to that in the m-ALFS-GC and m-GPFS-GC groups (Figure 9G,H). In contrast, the sham, GC, nm-GPFS-GC, and m-ROFS-GC groups showed a relatively higher number of round-shaped cells in comparison with those of fiber-oriented cells. As the PDL contains bundled collagen fibers and fibrils with various micro- and nanodiameters (Figures 2 and S5), we measured fiber diameters in the reformed PDL by TEM. In the implantation with and without GC or FHGC, TEM images exhibited a different fiber patterning in the reformed PDL (Figure 9I). The m-ALFS-GC group revealed a pattern of PDL fibers similar to the m-GPFS-GC group, and this fibrous structure differed from that in the sham, GC, or nm-GPFS-GC group. Both the m-ALFS-GC and m-GPFS-GC groups, but not other groups, also exhibited fiber numbers and diameters in the reformed PDL similar to those in the control group (Figure S13). Interestingly, the reformed PDL in the GC group showed that a greater number of fibers consisted of diameters between 30 and 50 nm, while the m-ROFS-GC group exhibited the presence of PDL fibers with relatively large diameters (between 70 and 130 nm).

4. DISCUSSION

While fiber patterning is a crucial factor in producing as-spun fibrous scaffolds, a classic or conventional electrospinning setup often limited the desired fiber patterning. Some notable characteristics of as-spun fibrous scaffolds can be induced by altering the chemistry of the materials applied.[27,28] The induction of ultrafine architectures such as spiderweb-like nanonets provides a versatile fiber platform for biomedical applications of high performance.[29,30] When a high voltage is supplied to polymer solutions supplemented with complex ions, solvents, drugs, and/or salts, the Taylor cone undergoes stretching, whipping, and solvent evaporation, eventually leading to nanonet fiber formation.[31] However, these methods not only limit the creation of nanonet fibers but also require additional steps to remove toxic agents from the products.[32] In contrast, the developed as-spun setup, named all-in-one electrospinning, is capable of producing desired and patterned nanonet and/or microfiber scaffolds on a single mat without the alteration of material chemistry and the use of any additives. First of all, this study not only demonstrates the advantage of the all-in-one electrospinning in manufacturing various types of as-spun scaffolds on a desired single mat but also highlights the optimized installations in inducing the nanonet fiber alignment of high performance.

The PDL matrix is a highly organized structure with different topographies depending on its location between the tooth and alveolar bone and provides PDLF with an appropriate microenvironment under compression or tensile force.[5] PDLFs respond sensitively to mechanical stimuli via the interaction with the fibrous matrix.[26,33,34] Therefore, morphology, behavior, and the function of PDLF are tightly affected by their location within the PDL, as well as by the structure of surrounding fibers such as Sharpey's and oxytalan fibers. Regarding the in vitro and in vivo results of m-ROFS, we postulate that unlikely to patterned scaffolds, a randomly oriented fiber structure does not exert the potentials derived from PDL-mimic fibrous scaffolds. It is important to note that the structure of PDL fibers is sensitively altered in response to a mechanical force (Figure S14A), in which the cross-links in collagen fibers and microfibrils are disrupted or condensed depending on compressive or tensile force application (Figure S14B). When a human tooth was exposed to compressive force on a punched TCP chamber (Figure S15B), some of the PDL collagen fibers showed a disrupted morphology (Figure S15B). More exactly, the PDL fibers exhibited an altered cross-linking and morphology of fibers and fibrils following the compression (Figure S15B). These results indicate that the application of compressive force may induce PDL with an abnormal and randomly oriented structure, like the morphology of m-ROFS. We previously found that dissimilar to tensile force, PDLF cultures under a compressive mechanical force preferably stimulated osteoclastic activation rather than osteogenic differentiation.[35] Our previous report also supported the roles of PDLF to facilitate alveolar bone absorption via the skewed expression of osteoclastogenic factors when the tooth is applied to compressive force.[36] These reports may explain why m-ROFS alone stimulated RANKL expression in cultured PDLF and enhanced the formation of multinucleated cells in the combined cultures with BMM. We also assume that the abnormal fibrous structure and cellular morphology in the reformed PDL of the m-ROFS-GC group are associated with fibrous morphology that occurs in a compression-applied PDL.

In addition to a collagenous matrix, PDL also contains various types of cells together with a few PDLSCs. The PDLFs are the most abundant PDL cells and secrete various surface markers that are expressed in undifferentiated cells.[14,37,38] Among the surface markers, CD105 is an MSC-derived PDLF-specific marker that is mainly expressed at early passage and gradually disappeared in relation to the passages.[39,40] Similarly, our results indicate that a stem-like proliferation of PDLF along with a high expression of CD105 is diminished following the passage and incubation times without the alteration of fibroblastic morphological characteristics. Our results suggest that PDLFs express the CD105 more highly than BMMSC during

https://doi.org/10.1021/acsami.2c18893
ACS Appl. Mater. Interfaces 2023, 15, 599−616

incubation at the same passage, and the patterned scaffolds maintain the potential of PDLF to express CD105 more than randomly oriented fiber. PDLFs also respond sensitively to compressive or tensile force and modulate alveolar bone remodeling via a balanced production of RANKL and its antagonist, osteoprotegerin.[36,41,42] In this regard, our results corroborate the potential of PDLF to proliferate and differentiate into mineralized or multinucleated osteoclastic cells depending on the culture conditions, although the osteogenic capacity of PDLF is not directly regulated by the fiber topographies of scaffolds.

Behaviors of PDLFs are sensitively affected by the structure of fibers that are attached to these cells. This means that fiber topography is the key effector in regulating mechanosignal-associated behaviors of PDLFs. Vinculin is a cytoskeletal protein enriched in adherent junctions and focal adhesions.[43] OPN and COLI are mechanosensitive proteins expressed highly in PDLF depending on the mechanical stress applied.[44,45] Specifically, YAP, a master transcriptional factor, regulates the expression of these mechanosensitive molecules.[46−49] Studies have demonstrated that YAP-associated signaling controls cellular proliferation, differentiation, and mechanosensing in relation to the topography and stiffness of fibers and mechanical force applied.[50,51] We also found previously that the expression of YAP and its cellular localization are the crucial factors to regulate cell behavior.[23,48,52] Similarly, our current findings indicate that as-spun scaffolds affect the behavior of PDLF differently in relation to their topographical cues, and these are tightly regulated by YAP and YAP-associated signaling.

The nuclear translocation of YAP is triggered by force via a regulation of transport across nuclear pores.[48] Cellular traction force together with the intensity and nuclear shuttling of YAP in cultured PDLF tended to be the important events to regulate behaviors. FAs regulate cell migration and comprise the linkage between integrin receptors and actions.[53] FAs are also the important sites of cell−matrix interaction. Periostin is essential for the function and integrity of PDL during mechanical loading, and its expression in PDLF is regulated by FA kinase.[54,55] These reports indicate that in addition to YAP, FA formation and periostin expression are essential factors in regulating the behaviors of PDLF in relation to the fiber topographies of scaffolds. In addition, our current findings strongly support that the formation and number of FAs and the expression pattern of periostin in PDLF are tightly regulated by YAP-associated signaling.

Alternatively, our findings indicated that the expression ratio of OPN in scaffold-seeded PDLF is approximately 1.8-fold higher than that of YAP, while BMMSCs show a similar ratio between these molecules. Even though it is not clear why OPN is expressed relatively higher in PDLF compared with YAP, there are some interesting reports. While YAP is the master regulator in controlling various cellular events, it also acts as a direct regulator and/or transcriptional coactivator in mediating cellular signaling in response to mechanical stimuli, fiber topographical cues, ECM rigidity, and cellular reprogramming.[46,47] More importantly, YAP is the key regulator in regulating proliferation, differentiation, and the migration of MSCs.[56,57] This indicates that YAP sensitively regulates cellular events even in a small quantity. Alternatively, OPN is initially reported to be expressed in osteoblasts, but numerous reports demonstrate its expression in PDLF, and it has important roles in tooth root development, proper formation and mineralization of dentin and alveolar bone, maintenance of dental pulp and PDL, and mechanoresponsive signaling.[45,58,59] In the periodontium, OPN also acts as a negative regulator of acellular hypermineralization, and this is associated with the phosphorylated level in the protein.[60] All of these reports postulate that OPN is an abundant protein in the periodontium and is expressed highly in response to the topographical cue of PDL fiber-representing scaffolds.

The water contact angle is an important factor in the transformation of a hydrophobic scaffold into a tunable hydrophilic scaffold, and this is affected by topography and the scale of fibers.[61,62] Here, we found a different contact angle among the as-spun scaffolds and FHGC along with the contact images corresponding to each of the scaffolds in a horizontal direction. Dissimilar to fibrous scaffolds, the ranges of contact angles in FHGC were between 50 and 80° indicating a water absorbency level within the range of ideal contact angles for the scaffolds that are applied in drug delivery and artificial tissues.[63] The m-ALFS-GC, nm-GPFS-GC, m-GPFS-GC, and m-ROFS-GC had water contact angles of 57.3, 58.4, 76.0, and 72.3°, respectively. These results indicate that the wetting transition energy barrier of the as-spun scaffolds is not a direct effector to regulate the behavior of PDLF, even though fiber topography-influenced wettability is known to affect protein adsorption and cell behavior.[64,65] Our results also suggest that the mechanical strength of FHGC in wet conditions is similar to that of in vivo conditions, in which any prominent differences among FHGC are not induced. Collectively, these physicochemical assays indicate that FHGC is a well-designed fiber−hydrogel complex and does not differ significantly in wettability and mechanical strength.

On the other hand, this study demonstrates that PDL regeneration is partially correlated with the formation of alveolar bone, where implantation with m-ALFS-GC, m-GPFS-GC, or m-ROFS-GC expresses greater effects than with nm-GPFS-GC or GC. Our results indicate that dissimilar to in vitro behaviors of PDLF, YAP expression and expression ratio of OPN to that of YAP are not directly associated with the repair or the morphological phenotypes of cells in the reformed PDL. Our findings also indicate that implantation with m-ALFS-GC or m-GPFS-GC, rather than GC, repairs the defected PDL more efficiently, and cells have a morphology that is common to native PDL. Namely, compared with nm-GPFS-GC, m-ROFS-GC, or GC, implantation with m-ALFS-GC or m-GPFS-GC may induce PDL fiber formation and patterning that has a greater similarity to that of native PDL. Moreover, our results imply that in addition to YAP-associated mechanosignaling, other molecules can be contributed to the gel complex-enhanced regeneration of PDL. However, it is important to note that the as-spun scaffolds, especially m-ALFS and m-GPFS, do not replace completely the anatomical properties of the native PDL matrix. The chemistry of native fibrous matrix might be also entirely different from that of as-spun scaffolds. Further experiments to fabricate collagenous scaffolds and 3D matrix gels that mimic native PDL matrix in chemistry, diameter, and orientation of fibers, as well as occupy PDL cells within the matrix, will be necessary. Additional experiments to verify whether the reformed PDL in the m-ALFS-GC and m-GPFS-GC groups functions at the periodontal interface in response to a mechanical stimulation will also be required for their application in dental clinics.

https://doi.org/10.1021/acsami.2c18893
ACS Appl. Mater. Interfaces 2023, 15, 599−616

5. CONCLUSIONS

Here, we developed an optimized all-in-one electrospinning setup with PDL-like fibrous scaffolds expressing Sharpey's fiber, oxytalan fiber, or both structures manufactured successfully on a single mat. This electrospinning method enabled controlled PDL fiber architectures with submicron resolution that depends on the mechanical force application through nanonet patterning. Compared with BMMSC, PDLF behaviors were tightly and specifically regulated in relation to the fiber topographical cues of the scaffolds. The fiber surface-dependent behaviors of PDLF were correlated with the expression of periodontal remodeling marker and mechanosensing molecules, in which YAP acted as the master regulator. Dissimilar to the aligned or grid/patterned microscale scaffold, disrupted PDL fibers occurred in the morphology of the patterned nanonets and randomly oriented fibrous scaffold and induced a skewed osteoclastic activation and an abnormal PDL reparation. Our findings supported a relationship between the potential of scaffolds to regulate PDLF behaviors and to regenerate defective PDL. Overall, this study demonstrated that m-ALFS and m-GPFS along with their hydrogel complexes are guided biomimetic and biocompatible scaffolds that can tightly regulate PDLF behaviors and regenerate damaged PDL effectively.

■ ASSOCIATED CONTENT

Supporting Information

The Supporting Information is available free of charge at https://pubs.acs.org/doi/10.1021/acsami.2c18893.

Preparation of human PDLF; assays for cell proliferation and differentiation; FTIR and XRD analyses of FSGCs; physical characterization of FSGCs; measurement of degradation property; experimental evaluation on the structural alteration of native PDL fibers in response to a compressive force; advantages of the developed electrospinning in patterned nanonet formation; and figures and legends for Figures S1−S15 (PDF)

■ AUTHOR INFORMATION

Corresponding Authors

Sung-Ho Kook − *Department of Bioactive Material Sciences, Research Center of Bioactive Materials, Jeonbuk National University, Jeonju 54896, South Korea;* orcid.org/0000-0002-1879-5927; Email: kooksh@jbnu.ac.kr; Fax: +82-63-270-3327

Jeong-Chae Lee − *Cluster for Craniofacial Development and Regeneration Research, Institute of Oral Biosciences and School of Dentistry, Jeonbuk National University, Jeonju 54896, South Korea; Department of Bioactive Material Sciences, Research Center of Bioactive Materials, Jeonbuk National University, Jeonju 54896, South Korea;* orcid.org/0000-0002-4340-7965; Email: jeongchae@jbnu.ac.kr; Fax: +82-63-270-4004

Authors

Jeong In Kim − *Cluster for Craniofacial Development and Regeneration Research, Institute of Oral Biosciences and School of Dentistry, Jeonbuk National University, Jeonju 54896, South Korea;* orcid.org/0000-0003-3753-0382

Ju Yeon Kim − *Department of Bionanosystem Engineering, Jeonbuk National University, Jeonju 54896, South Korea;* orcid.org/0000-0002-9029-3665

Govinda Bhattarai − *Cluster for Craniofacial Development and Regeneration Research, Institute of Oral Biosciences and School of Dentistry, Jeonbuk National University, Jeonju 54896, South Korea;* orcid.org/0000-0002-3789-3442

Han-Sol So − *Department of Bioactive Material Sciences, Research Center of Bioactive Materials, Jeonbuk National University, Jeonju 54896, South Korea;* orcid.org/0000-0003-0988-4685

Complete contact information is available at: https://pubs.acs.org/10.1021/acsami.2c18893

Author Contributions

J.I.K., S.-H.K., and J.-C.L. designed the electrospinning setup. J.I.K. and J.Y.K. fabricated scaffolds and fiber−hydrogel complexes and characterized their properties. J.I.K., G.B., H.-S.S., S.-H.K., and J.-C.L. cultured PDLF and BMMSC and analyzed their characteristics and behaviors. J.I.K., G.B., S.-H.K., and J.-C.L. performed in vivo experiments. J.I.K., S.-H.K., and J.-C.L. analyzed the data. J.I.K., G.B., S.-H.K., and J.-C.L. contributed reagents/materials/analysis tools. J.I.K., J.Y.K., S.-H.K., and J.-C.L. wrote and edited the manuscript. All authors reviewed the manuscript before submission.

Notes

The authors declare no competing financial interest.

■ ACKNOWLEDGMENTS

This work was supported by the Basic Science Research Program through the National Research Foundation of Korea funded by the Ministry of Science, Information and Communications Technology and Future Planning (2019R1A2C2084453, 2021R1A2C2006032, 2021R1I1AIA01044453, and 2021R1C1C2011469), South Korea.

■ REFERENCES

(1) Cardoso, E. M.; Reis, C.; Manzanares-Céspedes, M. C. Chronic Periodontitis, Inflammatory Cytokines, and Interrelationship with other Chronic Diseases. *Postgrad. Med.* **2018**, *130*, 98−104.

(2) Könönen, E.; Gursoy, M.; Gursoy, U. K. Periodontitis: A Multifaceted Disease of Tooth-Supporting Tissues. *J. Clin. Med.* **2019**, *8*, 1135.

(3) Hajishengallis, G.; Chavakis, T. Local and Systemic Mechanisms Linking Periodontal Disease and Inflammatory Comorbidities. *Nat. Rev. Immunol.* **2021**, *21*, 426−440.

(4) Rabelo, G. D.; de Paula, P. M.; Rocha, F. S.; Silva, C. J.; Zanetta-Barbosa, D. Retrospective Study of Bone Grafting Procedures Before Implant Placement. *Implant Dent.* **2010**, *19*, 342−350.

(5) de Jong, T.; Bakker, A. D.; Everts, V.; Smit, T. H. The Intricate Anatomy of the Periodontal Ligament and its Development: Lessons for Periodontal Regeneration. *J. Periodontal Res.* **2017**, *52*, 965−974.

(6) Alissa, R.; Oliver, R. Influence of Prognostic Risk Indicators on Osseointegrated Dental Implant Failure: A Matched Case-Control analysis. *J. Oral Implantol.* **2012**, *38*, 51−61.

(7) Sawada, T.; Sugawara, Y.; Asai, T.; Aida, N.; Yanagisawa, T.; Ohta, K.; Inoue, S. Immunohistochemical Characterization of Elastic System Fibers in Rat Molar Periodontal Ligament. *J. Histochem. Cytochem.* **2006**, *54*, 1095−1103.

(8) Aaron, J. E. Periosteal Sharpey's fibers: a Novel Bone Matrix Regulatory System? *Front. Endocrinol.* **2012**, *3*, 98.

(9) Li, C.; Fennessy, P. The Periosteum: a Simple Tissue with Many Faces, with Special Reference to the Antler-Lineage Periostea. *Biol. Direct* **2021**, *16*, No. 17.

(10) Kaku, M.; Yamauchi, M. Mechano-regulation of Collagen Biosynthesis in Periodontal Ligament. *J. Prosthodont. Res.* **2014**, *58*, 193−207.

(11) Lekic, P.; McCulloch, C. A. Periodontal Ligament Cell Populations: The Central Role of Fibroblasts in Creating a Unique Tissue. *Anat. Rec.* **1996**, *245*, 327−341.
(12) Marchesan, J. T.; Scanlon, C. S.; Soehren, S.; Matsuo, M.; Kapila, Y. L. Implications of Cultured Periodontal Ligament Cells for the Clinical and Experimental Setting: a Review. *Arch. Oral Biol.* **2011**, *56*, 933−943.
(13) Zhu, W.; Liang, M. Periodontal Ligament Stem Cells: Current Status, Concerns, and Future Prospects. *Stem Cells Int.* **2015**, *2015*, 1−11.
(14) Lim, S. S.; Kook, S. H.; Lee, J. C. COMP-Ang1 Enhances DNA Synthesis and Cell Cycle Progression in Human Periodontal Ligament Cells via Tie2-Mediated Phosphorylation of PI3K/Akt and MAPKs. *Mol. Cell. Biochem.* **2016**, *416*, 157−168.
(15) Wang, Z. S.; Feng, Z. H.; Wu, G. F.; Bai, S. Z.; Dong, Y.; Chen, F. M.; Zhao, Y. M. The Use of Platelet-Rich Fibrin Combined with Periodontal Ligament and Jaw Bone Mesenchymal Stem Cell Sheets for Periodontal Tissue Engineering. *Sci. Rep.* **2016**, *6*, No. 28126.
(16) Li, Y.; Zhan, Q.; Bao, M.; Yi, J.; Li, Y. Biomechanical and Biological Responses of Periodontium in Orthodontic Tooth Movement: Up-date in a New Decade. *Int. J. Oral Sci.* **2021**, *13*, No. 20.
(17) Wang, X.; Jin, J.; Hou, R.; Zhou, M.; Mou, X.; Xu, K.; Zhu, Y.; Shen, Z.; Zhang, X. Differentiation of bMSCs on Biocompatible, Biodegradable, and Biomimetic Scaffolds for Largely Defected Tissue Repair. *ACS Appl. Bio Mater.* **2020**, *3*, 735−746.
(18) Gaharwar, A. K.; Singh, I.; Khademhosseini, A. Engineered Biomaterials for In Situ Tissue Regeneration. *Nat. Rev. Mater.* **2020**, *5*, 686−705.
(19) Won, J. E.; Lee, Y. S.; Park, J. H.; Lee, J. H.; Shin, Y. S.; Kim, C. H.; Knowles, J. C.; Kim, H. W. Hierarchical Microchanneled Scaffolds Modulate Multiple Tissue-Regenerative Processes of Immune-Responses, Angiogenesis, and Stem Cell Homing. *Biomaterials* **2020**, *227*, No. 119548.
(20) Vaquette, C.; Fan, W.; Xiao, Y.; Hamlet, S.; Hutmacher, D. W.; Ivanovski, S. A Biphasic Scaffold Design Combined with Cell Sheet Technology for Simultaneous Regeneration of Alveolar Bone/Periodontal Ligament Complex. *Biomaterials* **2012**, *33*, 5560−5573.
(21) Xu, X. Y.; LI, X.; Wang, J.; He, X. T.; Sun, H. H.; Chen, F. M. Concise Review: Periodontal Tissue Regeneration Using Stem Cells: Strategies and Translational Considerations. *Stem Cells Transl. Med.* **2019**, *8*, 392−403.
(22) Liang, Y.; Luan, X.; Liu, X. Recent Advances in Periodontal Regeneration: A Biomaterial Perspective. *Bioact. Mater.* **2020**, *5*, 297−308.
(23) Kim, J. I.; Kim, J. Y.; Kook, S. H.; Lee, J. C. A Novel Electrospinning Method for Self-Assembled Tree-like Fibrous Scaffolds: Microenvironment-Associated Regulation of MSC Behavior and Bone Regeneration. *J. Mater. Sci. Technol.* **2022**, *115*, 52−70.
(24) Tonti, O. R.; Larson, H.; Lipp, S. N.; Luetkemeyer, C. M.; Makam, M.; Vargas, D.; Wilcox, S. M.; Calve, S. Tissue-Specific Parameters for the Design of ECM-Mimetic Biomaterials. *Acta Biomater.* **2021**, *132*, 83−102.
(25) Doolin, M. T.; Ornstein, T. S.; Stroka, K. M. Nuclear Deformation in Response to Mechanical Confinement is Cell Type Dependent. *Cells* **2019**, *8*, 427.
(26) Kook, S. H.; Son, Y. O.; Hwang, J. M.; Kim, E. M.; Lee, C. B.; Jeon, Y. M.; Kim, J. G.; Lee, J. C. Mechanical Force Inhibits Osteoclastogenic Potential of Human Periodontal Ligament Fibroblasts Through OPG Production and ERK-Mediated Signaling. *J. Cell. Biochem.* **2009**, *106*, 1010−1019.
(27) Cho, S. H.; Kim, J. I.; Kim, C. S.; Park, C. H.; Kim, I. G. Harnessing the Topography of 3D Spongy-Like Electrospun Bundled Fibrous Scaffold via a Sharply Inclined Array Collector. *Polymers* **2019**, *11*, 1444.
(28) Liu, S.; Qin, S.; He, M.; Zhou, D.; Qin, Q.; Wang, H. Current Applications of Poly(Lactic Acid) Composites in Tissue Engineering and Drug Delivery. *Composites, Part B* **2020**, *199*, No. 108238.
(29) Kim, H. J.; Pant, H.; Park, C. H.; Tijing, L.; Hwang, B. S.; Choi, N.; Kim, C. S. Electrical Properties of ZnO/Nylon-6 Spider-Wave-like Nanonets Prepared via Electrospinning. *Dig. J. Nanomater. Biostruct.* **2013**, *8*, 385−393.
(30) Zhang, S.; Liu, H.; Yin, X.; Li, Z.; Yu, J.; Ding, B. Tailoring Mechanically Robust Poly (m-Phenylene Isophthalamide) Nanofiber/nets for Ultrathin High-Efficiency Air Filter. *Sci. Rep.* **2017**, *7*, No. 40550.
(31) Saudi, S.; Bhattarai, S. R.; Adhikari, U.; Khanal, S.; Sankar, J.; Aravamudhan, S.; Bhattarai, N. Nanonet-Nano Fiber Electrospun Mesh of PCL-Chitosan for Controlled and Extended Release of Diclofenac Sodium. *Nanoscale* **2020**, *12*, 23556−23569.
(32) Wang, X.; Ding, B.; Sun, G.; Wang, M.; Yu, J. Electro-spinning/Netting: A Strategy for the Fabrication of Three-Dimensional Polymer Nano-Fiber/Nets. *Prog. Mater. Sci.* **2013**, *58*, 1173−1243.
(33) Grandfield, K.; Herber, R. P.; Chen, L.; Djomehri, S.; Tam, C.; Lee, J. H.; Brown, E.; Woolwine, W. R., 3rd; Curtis, D.; Ryder, M.; Schuck, J.; Webb, S.; Landis, W.; Ho, S. Strain-Guided Mineralization in the Bone-PDL-Cementum Complex of a Rat Periodontium. *Bone Rep.* **2015**, *3*, 20−31.
(34) Jiang, N.; Guo, W.; Chen, M.; Zheng, Y.; Zhou, J.; Kim, S. G.; Embree, M. C.; Song, K. S.; Marao, H. F.; Mao, J. J. Periodontal Ligament and Alveolar Bone in Health and Adaptation: Tooth Movement. In *Frontiers of Oral Biology*; S. Karger: Basel, 2015; Vol. *18*, pp 1−8 DOI: 10.1159/000351894.
(35) Sokos, D.; Everts, V.; de Vries, T. J. Role of Periodontal Ligament Fibroblasts in Osteoclastogenesis: A Review. *J. Periodontal Res.* **2015**, *50*, 152−159.
(36) Kook, S. H.; Jang, Y. S.; Lee, J. C. Human Periodontal Ligament Fibroblasts Stimulate Osteoclastogenesis in Response to Compression Force through TNF-α-Mediated Activation of CD4+ T Cells. *J. Cell. Biochem.* **2011**, *112*, 2891−2901.
(37) Seo, B. M.; Miura, M.; Gronthos, S.; Bartold, P. M.; Batouli, S.; Brahim, J.; Young, M.; Robey, P. G.; Wang, C. U.; Shi, S. Investigation of Multipotent Postnatal Stem Cells from Human Periodontal Ligament. *Lancet* **2004**, *364*, 149−155.
(38) Iwata, T.; Yamato, M.; Tsuchioka, H.; Takagi, R.; Mukobata, S.; Washio, K.; Okano, T.; Ishikawa, I. Periodontal Regeneration with Multi-Layered Periodontal Ligament-Derived Cell Sheets in a Canine Model. *Biomaterials* **2009**, *30*, 2716−2723.
(39) Lee, H. J.; Choi, B. H.; Min, B. H.; Park, S. R. Changes in Surface Markers of Human Mesenchymal Stem Cells During the Chondrogenic Differentiation and Dedifferentiation Processes In Vitro. *Arthritis Rheum.* **2009**, *60*, 2325−2332.
(40) Xu, J.; Wang, W.; Kapila, Y.; Lotz, J.; Kapila, S. Multiple Differentiation Capacity of STRO-1+/CD146+ PDL Mesenchymal Progenitor Cells. *Stem Cells Dev.* **2009**, *18*, 487−496.
(41) Cao, X. RANKL-RANK Signaling Regulates Osteoblast Differentiation and Bone Formation. *Bone Res.* **2018**, *6*, No. 35.
(42) Li, M.; Zhang, C.; Yang, Y. Effects of Mechanical Forces on Osteogenesis and Osteoclastogenesis in Human Periodontal Ligament Fibroblasts: A Systematic Review of In Vitro Studies. *Bone Joint Res.* **2019**, *8*, 19−31.
(43) Bays, J. L.; DeMali, K. S. Vinculin in Cell−Cell and Cell−Matrix Adhesions. *Cell. Mol. Life Sci.* **2017**, *74*, 2999−3009.
(44) Hudson, D. M.; Garibov, M.; Dixon, D. R.; Popowics, T.; Eyre, D. R. Distinct Post-Translational Features of Type I Collagen are Conserved in Mouse and Human Periodontal Ligament. *J. Periodontal Res.* **2017**, *52*, 1042−1049.
(45) Foster, B. L.; Ao, M.; Salmon, C. R.; Chavez, M. B.; Kolli, T. N.; Tran, A. B.; Chu, E. Y.; Kantovitz, K. R.; Yadav, M.; Narisawa, S.; Millán, J. L.; Nociti, F. H., Jr.; Somerman, M. J. Osteopontin Regulates Dentin and Alveolar Bone Development and Mineralization. *Bone* **2018**, *107*, 196−207.
(46) Dupont, S.; Morsut, L.; Aragona, M.; Enzo, E.; Giulitti, S.; Cordenonsi, M.; Zanconato, F.; Digabel, J. L.; Forcato, M.; Bicciato, S.; Elvassore, N.; Piccolo, S. Role of YAP/TAZ in Mechanotransduction. *Nature* **2011**, *474*, 179−185.
(47) Dupont, S. Role of YAP/TAZ in Cell-Matrix Adhesion-Mediated Signalling and Mechanotransduction. *Exp. Cell Res.* **2016**, *343*, 42−53.

(48) Elosegui-Artola, A.; Andreu, I.; Beedle, A.; Lezamiz, A.; Uroz, M.; Kosmalska, A.; Oria, R.; Kechagia, J. Z.; Rico-Lastres, P.; Le Roux, A. -L.; Shanahan, C.; Trepat, X.; Navajas, D.; Garcia-Manyes, S.; Roca-Cusachs, P. Force Triggers YAP Nuclear Entry by Regulating Transport across Nuclear Pores. *Cell* **2017**, *171*, 1397−1410.
(49) Bonnevie, E. D.; Ashinsky, B. G.; Dekky, B.; Volk, S. W.; Smith, H. E.; Mauck, R. L. Cell Morphology and Mechanosensing can be Decoupled in Fibrous Microenvironments and Identified Using Artificial Neural Networks. *Sci. Rep.* **2021**, *11*, No. 5950.
(50) Yang, C.; Tibbitt, M. W.; Basta, L.; Anseth, K. S. Mechanical Memory and Dosing Influence Stem Cell Fate. *Nat. Mater.* **2014**, *13*, 645−652.
(51) Shiu, J. Y.; Aires, L.; Lin, Z.; Vogel, V. Nanopillar Force Measurements Reveal Actin-Cap-Mediated YAP Mechanotransduction. *Nat. Cell Biol.* **2018**, *20*, 262−271.
(52) Kim, J. I.; Hwang, T. I.; Lee, J. C.; Park, C. H.; Kim, C. S. Regulating Electrical Cue and Mechanotransduction in Topological Gradient Structure Modulated Piezoelectric Scaffolds to Predict Neural Cell Response. *Adv. Funct. Mater.* **2020**, *30*, No. 1907330.
(53) Humphries, J. D.; Wang, P.; Streuli, C.; Geiger, B.; Humphries, M. J.; Ballestrem, C. Vinculin Controls Focal Adhesion Formation by Direct Interactions with Talin and Actin. *J. Cell. Biol.* **2007**, *179*, 1043−1057.
(54) Rios, H. F.; Ma, D.; Xie, Y.; Giannobile, W. V.; Bonewald, L. F.; Conway, S. J.; Feng, J. Q. Periostin is Essential for the Integrity and Function of the Periodontal Ligament During Occlusal Loading in Mice. *J. Periodontal* **2008**, *79*, 1480−1490.
(55) Wen, W.; Chau, E.; Jackson-Boeters, L.; Elliott, C.; Daley, T. D.; Hamilton, D. W. TGF-β1 and FAK Regulate Periostin Expression in PDL Fibroblasts. *J. Dent. Res.* **2010**, *89*, 1439−1443.
(56) Mascharak, S.; Benitez, P. L.; Proctor, A. C.; Madl, C. M.; Hu, K. H.; Dewi, R. E.; Butte, M. J.; Heilshorn, S. C. YAP-Dependent Mechanotransduction is Required for Proliferation and Migration on Native-like Substrate Topography. *Biomaterials* **2017**, *115*, 155−166.
(57) Pan, J. X.; Xiong, L.; Zhao, K.; Zeng, P.; Wang, B.; Tang, F. L.; Sun, D.; Guo, H. H.; Yang, X.; Cui, S.; Xia, W. F.; Mei, L.; Xiong, W. C. YAP Promotes Osteogenesis and Suppresses Adipogenic Differentiation by Regulating beta-Catenin Signaling. *Bone Res.* **2018**, *6*, 18.
(58) Wongkhantee, S.; Yongchaitrakul, T.; Pavasant, P. Mechanical Stress Induces Osteopontin Expression in Human Periodontal Ligament Cells through Rho Kinase. *J. Periodontol.* **2007**, *78*, 1113−1119.
(59) Chaikiawkeaw, D.; Khorattanakulchai, N.; Nammultriputtar, K.; Rattanapisit, K.; Everts, V.; Kubera, A.; Phoolchareon, W.; Pavasant, P. Osteopontin Induces Osteogenic Differentiation by Human Periodontal Ligament Cells via Calcium Binding Domain-Activin Receptor-like Kinase (ALK-1) Interaction. *J. Periodontol.* **2022**, *93*, e13−e23.
(60) Gericke, A.; Qin, C.; Spevak, L.; Fujimoto, Y.; Butler, W. T.; Sørensen, E. S.; Boskey, A. L. Importance of Phosphorylation for Osteopontin Regulation of Biomineralization. *Calcif. Tissue Int.* **2005**, *77*, 45−54.
(61) Sadeghi, A.; Moztarzadeh, F.; Mohandesi, J. A. Investigating the Effect of Chitosan on Hydrophilicity and Bioactivity of Conductive Electrospun Composite Scaffold for Neural Tissue Engineering. *Int. J. Biol. Macromol.* **2019**, *121*, 625−632.
(62) Lanno, G. M.; Ramos, C.; Preem, L.; Putrins, M.; Laidmae, I.; Tenson, T.; Kogermann, K. Antibacterial Porous Electrospun Fibers as Skin Scaffolds for Wound Healing Applications. *ACS Omega* **2020**, *5*, 30011−30022.
(63) Menzies, K. L.; Jones, L. The Impact of Contact Angle on the Biocompatibility of Biomaterials. *Optom. Vis. Sci.* **2010**, *87*, 387−399.
(64) Kim, J. I.; Kim, J. Y.; Park, C. H. Fabrication of Transparent Hemispherical 3D Nanofibrous Scaffolds with Radially Aligned Patterns via a Novel Electrospinning Method. *Sci. Rep.* **2018**, *8*, No. 3424.
(65) Kim, J. I.; Kim, C. S. Nanoscale Resolution 3D Printing with Pin-Modified Electrified Inkjets for Tailorable Nano/Macrohybrid Constructs for Tissue Engineering. *ACS Appl. Mater. Interfaces* **2018**, *10*, 12390−12405.

https://doi.org/10.1021/acsami.2c18893
ACS Appl. Mater. Interfaces 2023, 15, 599−616